

## THE *CHANDRA* LOCAL VOLUME SURVEY: THE X-RAY POINT SOURCE POPULATION OF NGC 404

B. BINDER<sup>1</sup>, B. F. WILLIAMS<sup>1</sup>, M. ERACLEOUS<sup>2</sup>, T. J. GAETZ<sup>3</sup>, A. K. H. KONG<sup>4</sup>, E. D. SKILLMAN<sup>5</sup>, D. R. WEISZ<sup>1</sup>

*Draft version June 29, 2021*

### ABSTRACT

We present a comprehensive X-ray point source catalog of NGC 404 obtained as part of the *Chandra* Local Volume Survey. A new, 97 ks *Chandra* ACIS-S observation of NGC 404 was combined with archival observations for a total exposure of  $\sim 123$  ks. Our survey yields 74 highly significant X-ray point sources and is sensitive to a limiting unabsorbed luminosity of  $\sim 6 \times 10^{35}$  erg s<sup>-1</sup> in the 0.35-8 keV band. To constrain the nature of each X-ray source, cross-correlations with multi-wavelength data were generated. We searched overlapping *HST* observations for optical counterparts to our X-ray detections, but find only two X-ray sources with candidate optical counterparts. We find 21 likely low mass X-ray binaries (LMXBs), although this number is a lower limit due to the difficulties in separating LMXBs from background AGN. The X-ray luminosity functions (XLFs) in both the soft and hard energy bands are presented. The XLFs in the soft band (0.5-2 keV) and the hard band (2-8 keV) have a limiting luminosity at the 90% completeness limit of  $10^{35}$  erg s<sup>-1</sup> and  $10^{36}$  erg s<sup>-1</sup>, respectively, significantly lower than previous X-ray studies of NGC 404. We find the XLFs to be consistent with those of other X-ray populations dominated by LMXBs. However, the number of luminous ( $> 10^{37}$  erg s<sup>-1</sup>) X-ray sources per unit stellar mass in NGC 404 is lower than is observed for other galaxies. The relative lack of luminous XRBs may be due to a population of LMXBs with main sequence companions formed during an epoch of elevated star formation  $\sim 0.5$  Gyr ago.

*Subject headings:* surveys — binaries: general — galaxies: individual (NGC 404) — surveys: X-rays: galaxies

### 1. INTRODUCTION

The X-ray emission from non-active, early type galaxies is dominated by hot gas (Canizares et al. 1987; O’Sullivan et al. 2001) and the X-ray binary (XRB) population. XRBs contain a compact object – either a neutron star (NS) or black hole (BH) – accreting from a stellar companion. In low mass XRBs (LMXBs), the companion star is of type A or later, while high mass XRBs (HMXBs) have O or B type companions. Due to the short lifetimes of high mass stars, HMXBs are observed to trace regions of recent star formation (Shtykovskiy & Gilfanov 2007), while the longer-lived lower mass companions of LMXBs follow the underlying, older stellar populations of the host galaxy (Kong et al. 2002; Soria & Kong 2002; Trudolyubov et al. 2002). Thus, the ensemble properties of a galaxy’s X-ray point source population, such as the X-ray luminosity function (XLF), should correlate with the star formation history (SFH) and morphology of the host galaxy (Grimm et al. 2003; Belczynski et al. 2004; Eracleous et al. 2006).

The *Chandra* Local Volume Survey is a deep, volume-limited survey of five nearby galaxies (NGC 55, NGC 300, NGC 404, NGC 2403, and NGC 4214) with overlapping *Hubble Space Telescope* (*HST*) observations (down

to  $M_V \sim 0$ , Dalcanton et al. 2009), designed to test correlations between the shape of the XLF and SFH of the host galaxy. When combined with the already well-studied disks of M 31 (Kong & Di Stefano 2003) and M 33 (Tüllmann et al. 2011; Plucinsky et al. 2008; Williams et al. 2008) available in the literature, these galaxies contain  $\sim 99\%$  of the extragalactic stellar mass and  $\sim 90\%$  of the recent star formation out to  $\sim 3.3$  Mpc (Tikhonov et al. 2003; Maíz-Apellániz et al. 2002). These galaxies additionally span a representative sample of disk galaxies with a range of masses, morphologies, and metallicities. With its excellent angular resolution ( $\sim 0''.5$ ) and positional accuracy, *Chandra* is the only X-ray telescope capable of separating the X-ray point source populations of nearby galaxies (out to a few Mpc) from diffuse emission. Our collaboration has already examined the X-ray point source population of NGC 300 in Binder et al. (2012), hereafter referred to as Paper I.

In this paper, we present the results of a new *Chandra* observation of NGC 404. At 3.05 Mpc (Dalcanton et al. 2009), NGC 404 is the closest face-on ( $i = 11^\circ$ , del Río et al. 2004) S0 galaxy to the Milky Way. Although its optical morphology suggests NGC 404 is a classic “red and dead” early-type galaxy, the center appears to have a significant young component (Bouchard et al. 2010; Seth et al. 2010; Thilker et al. 2010; Maoz et al. 1998) and may host an intermediate-mass, low-luminosity active nucleus (LLAGN, Binder et al. 2011; Seth et al. 2010; Maoz et al. 2005; Eracleous et al. 2002). Here, we focus on the non-nuclear X-ray point source population; the central source is included as part of the X-ray source catalog, but is not discussed in detail in the work (for a discussion of this source, see Binder et al. 2011).

The organization of this paper is as follows. In Sec-

<sup>1</sup> University of Washington, Department of Astronomy, Box 351580, Seattle, WA 98195

<sup>2</sup> Department of Astronomy & Astrophysics and Center for Gravitational Wave Physics, The Pennsylvania State University, 525 Davey Lab, University Park, PA 16802

<sup>3</sup> Harvard-Smithsonian Center for Astrophysics, 60 Garden Street Cambridge, MA 02138, USA

<sup>4</sup> Institute of Astronomy and Department of Physics, National Tsing Hua University, Hsinchu 30013, Taiwan

<sup>5</sup> University of Minnesota, Astronomy Department, 116 Church St. SE, Minneapolis, MN 55455

tion 2 we provide the details of the new observations, the archival data, as well as an outline of our data reduction process and the technique used to generate the X-ray source catalog. Section 3 provides an analysis of the X-ray source catalog, including hardness ratios, timing analysis, spectral fitting for bright sources, and the optical counterpart identification. The XLF and connection to the underlying SFH of NGC 404 is discussed in Section 5. We conclude with a discussion and summary in Section 6.

## 2. OBSERVATIONS AND DATA REDUCTION

### 2.1. Observations and Image Alignment

NGC 404 was observed during the *Chandra* X-ray Observatory Cycle 12 on 2010 October 21-22 for 97 ks using the ACIS-S array (Obs. ID 12339), with the nucleus nearly centered on the nominal aim point of the S3 chip. We additionally utilize archival observations: NGC 404 was observed on 1999 December 19 (Obs. ID 870) for  $\sim 24$  ks and on 2000 August 30 (Obs. ID 384) for  $\sim 2$  ks, both using the ACIS-S array. Table 1 summarizes the *Chandra* observations used in this work.

Data reduction was performed using CIAO v4.3 and CALDB v4.4.2 using standard reduction procedures. All observations were reprocessed from evtl level files using the CIAO routine `acis_process_events` with default parameters. The data were corrected for bad pixels/columns, charge transfer inefficiency, and time-dependent gain variations, and we removed the pixel randomization. The event list was then filtered for grades = 0, 2, 3, 4, 6, status = 0, and the pipeline-provided good time intervals. We checked for background flares by creating a background light curve and the source-free event lists on the S3 chip in each observation, and applied a sigma-clipping algorithm to remove time intervals with count rates more than  $3\sigma$  from the mean. Exposure maps and exposure-corrected images were made using `fluximage` and observations were then merged using `reproject_image`. Spectral weights used for the instrument maps were generated assuming a power law spectrum with  $\Gamma = 1.9$  (appropriate for both XRBs and background AGN), and the average foreground column density  $N_{\text{H}} = 5.13 \times 10^{20} \text{ cm}^{-2}$  (Kalberla et al. 2005) was used.

We created images in the following energy bands (keV): 0.35-8.0, 0.35-1.0, 1.0-2.0, 2.0-8.0 with bin sizes of 1, 2, 3, and 4. A composite X-ray image of NGC 404 is shown in Figure 1; soft X-rays (0.35-1.0 keV) are displayed in red, medium-hard X-ray emission (1-2 keV) is shown in green, and hard X-rays (2-8 keV) are shown in blue. The optical extent of the galaxy is superimposed in white. The combined exposure map for all three NGC 404 observations is shown in Figure 2.

Three *HST* fields were used to search for optical counterparts for each of our X-ray sources. One field (labeled ‘DEEP’) was taken as part of the Advanced Camera for Surveys (ACS) Nearby Galaxy Survey Treasury (ANGST, GO-10915 Dalcanton et al. 2009), while the other two shallower fields (labeled ‘NE’ and ‘SW’) were obtained as part of GO-11986. Details of the *HST* data acquisition and data reduction are provided in Williams et al. (2010). Figure 3 shows the locations of our *HST* fields and *Chandra* X-ray point sources superimposed on

a *GALEX* image of NGC 404.

To identify candidate optical counterparts to our *Chandra* X-ray sources, we place both the *Chandra* and *HST* fields onto the International Celestial Reference System (ICRS) by finding matches (within  $\sim 5''$ ) between stars or background galaxies in the Two Micron All Sky Survey (2MASS) Point Source Catalog (Skrutskie et al. 2006). We were able to identify 3-4 bright 2MASS sources per field which matched either a *Chandra* X-ray source or optical foreground star or background galaxy. The plate solutions were computed using the IRAF task `ccmap`, with *rms* residuals typically less than a few hundredths of an arcsecond in both right ascension and declination. The total alignment error applied to each X-ray source within a given field were computed by summing the *Chandra* and *HST* *rms* errors in quadrature. The results of our astrometry are summarized in Table 2.

### 2.2. Source Catalog Creation

We employed the same iterative source detection strategy as in Paper I (see also Tüllmann et al. 2011). We present a summary of the approach here; the reader is referred to Paper I and Tüllmann et al. (2011) for details. Additionally, we provide a direct comparison of this iterative source detection strategy to the more traditional approach of using the CIAO task `wavdetect` (Freeman et al. 2002) in the Appendix.

The CIAO task `wavdetect` (Freeman et al. 2002) was first used to create a list of potential source candidates to be used as input to ACIS-Extract (AE; Broos et al. 2010). AE is a source extraction and characterization tool which was used to determine various source properties (source and background count rates, detection significances, fluxes, etc.) and to generate light curves and spectra (with appropriate response matrices). We use the Poisson probability of not being a source (*prob.no.source*; hereafter *pns*) provided by AE as our threshold criteria when constructing the NGC 404 point source catalog.

For each input source, AE creates background regions by first removing all sources from the data and then searching for the smallest circular region around each source that encompasses at least the minimum number of background counts specified by the user. We require each background area to contain at least 50 counts (Tüllmann et al. 2011, found that changing the number of background counts required from 50 to 100 does not significantly affect source properties). These circular background regions are additionally the regions used to extract background spectra. To extract the X-ray spectrum for each source, AE constructs a polygon region that approximates the 90% contour of the *Chandra*-ACIS PSF at the location of the source. The CIAO tools `mkacisrmf` and `mkarf` are used to create appropriate response and ancillary response matrices for each source.

The initial source list generated by `wavdetect` was deliberately made to include many more sources (762) than we anticipated being statistically significant. We then applied the iterative procedure described in Paper I and Tüllmann et al. (2011) to remove false sources. Our final iteration required that a candidate X-ray source have  $pns < 4 \times 10^{-6}$  (see also Nandra et al. 2005; Georgakakis et al. 2008; Tüllmann et al. 2011) in any of the following energy bands: 0.5-8, 0.5-2, 2-8, 0.5-1, 1-2, 2-4, 4-8,

TABLE 1  
 SUMMARY OF *Chandra* OBSERVATIONS

Obs. ID (1)	Date (2)	Exposure (ks) (3)	R.A. (J2000) (4)	Decl. (J2000) (5)
384	1999 Aug 30	1.8	01 <sup>h</sup> 09 <sup>m</sup> 26 <sup>s</sup> .90	+35 <sup>d</sup> 43 <sup>m</sup> 03 <sup>s</sup> .00
870	2000 Dec 19	24	01 <sup>h</sup> 09 <sup>m</sup> 26 <sup>s</sup> .90	+35 <sup>d</sup> 43 <sup>m</sup> 03 <sup>s</sup> .40
12239	2010 Oct 21-22	97	01 <sup>h</sup> 09 <sup>m</sup> 27 <sup>s</sup> .00	+35 <sup>d</sup> 43 <sup>m</sup> 04 <sup>s</sup> .00

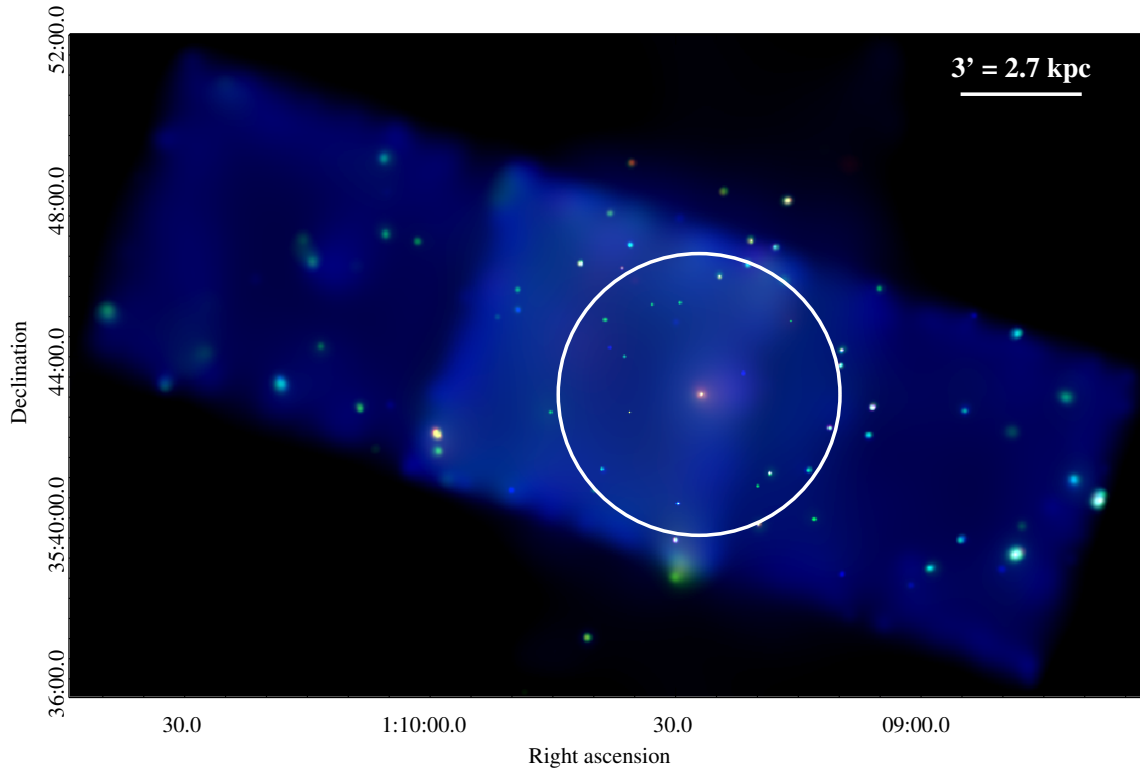


FIG. 1.— Multicolor exposure-corrected X-ray image of NGC 404. Red represents soft X-ray emission (0.35-1 keV), green represents medium-hard X-rays (1-2 keV), and blue denotes hard X-rays (2-8 keV). The white circle shows the optical extent of the galaxy ( $D_{25}$ , with a radius of  $3.5 = 3.1$  kpc).

 TABLE 2  
 ALIGNMENT OF *Chandra* AND *HST* OBSERVATIONS TO 2MASS

Observatory (1)	Field (2)	# Sources Used for Alignment (3)	R. A. $rms^a$ (4)	Decl. $rms^a$ (5)	# X-ray Sources (6)
<i>Chandra</i>	merged	3	0''049	0''087	74
<i>HST</i>	DEEP (Obs. ID 10915)	3	0''066 (0''082)	0''030 (0''042)	3
<i>HST</i>	NE (Obs. ID 11986)	4	0''041 (0''064)	0''017 (0''034)	5
<i>HST</i>	SW (Obs. ID 11986)	4	0''088 (0''100)	0''001 (0''087)	3

NOTE. — <sup>a</sup>The  $rms$  values listed are for each individual *HST* field. In parentheses we list the combined  $rms$  value for each field, obtained by adding the *Chandra* and *HST*  $rms$  values in quadrature.

0.35-1, or 0.35-8 keV.

The final CLVS source catalog for NGC 404 contains 74 sources<sup>6</sup>. Their positions and properties, such as detection significance ( $pns$  value), net counts, and photon fluxes (in eight different energy bands) are listed in Tables 3-6. Both Georgakakis et al. (2008) and Tüllmann

et al. (2011) have found that using a  $pns$  threshold of  $4 \times 10^{-6}$  results in  $\sim 0.5$  false sources per megapixel. Given the survey size of our NGC 404 observations, we expect there to be  $\sim 1.6$  false sources included in our final source catalog.

### 2.3. Sensitivity Maps

Subsequent analyses in this work require sensitivity maps, which provide the energy flux level at which a

<sup>6</sup> The source catalog is available in FITS format at <http://www.astro.washington.edu/users/bbinder/CLVS/>

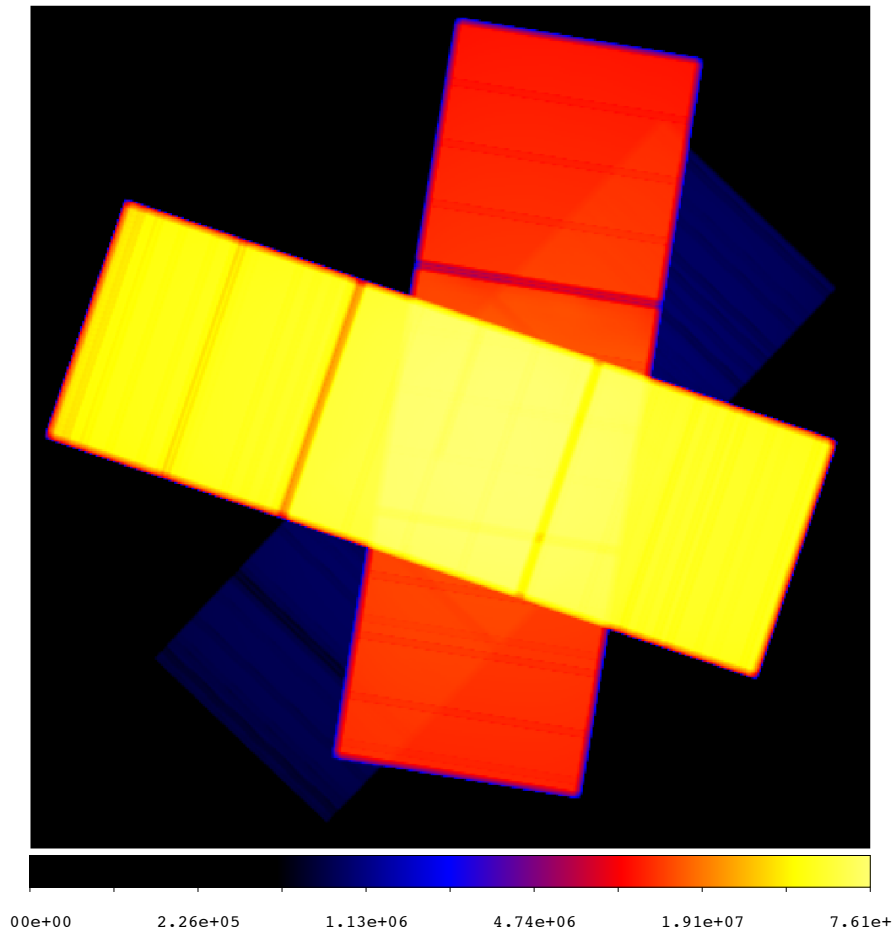


FIG. 2.— Combined exposure map for all three observations of NGC 404, shown on a logarithmic scale, in units of  $\text{cm}^2 \text{ s}$ .

TABLE 3  
THE NGC 404 SOURCE LIST

Source No.	Source ID	R.A. (J2000) ( $^\circ$ )	Decl. (J2000) ( $^\circ$ )	Positional Error ( $''$ )	Total exp. map value ( $\text{s cm}^2$ )	$R_{\text{src}}$ (sky pixel)	$\theta$ ( $'$ )
(1)	(2)	(3)	(4)	(5)	(6)	(7)	(8)
1	010838.25+354027.3	17.159396	35.674264	0.23	$3.803 \times 10^7$	21.68	10.0
2	010841.45+354056.8	17.172710	35.682458	0.47	$4.848 \times 10^7$	19.21	9.3
3	010842.38+354300.8	17.176591	35.716903	0.55	$4.835 \times 10^7$	17.38	8.9
4	010847.72+353948.3	17.198868	35.663419	0.69	$4.904 \times 10^7$	15.91	8.4
5	010848.00+354437.4	17.200024	35.743725	0.37	$3.429 \times 10^7$	5.54	7.9

NOTE. — Column 2: the source ID also contains the source coordinates (J2000.0). Column 5: the positional uncertainty is a simple error circle (in  $''$ ) around the source R.A. and decl. Column 6: sum of mean exposure map values in the source region. Column 7: the average radius of the source extraction region (1 sky pixel =  $0''.392$ ). Column 8: off-axis angle. Only the first five entries are shown.

source could be detected for each point in our survey area. AE provides an estimate of the photon flux for each source (*flux2*), which is based on the net source counts, exposure time, and the mean ARF in the given energy band. We convert these photon fluxes to energy fluxes assuming a power law with  $\Gamma = 1.9$  that is absorbed by the Galactic column ( $N_{\text{H}} = 5.13 \times 10^{20} \text{ cm}^{-2}$ ). Hereafter, we refer to this as the “standard model.” Roughly 80% of our X-ray sources had their spectra automatically fit with AE (see Section 3.4), and most were consistent with a power law model ( $\Gamma \sim 1.7\text{--}1.9$ ) with no absorption beyond the Galactic column, as would be expected for a

population dominated by XRBs and background AGN. We do not expect the standard model to systematically bias the  $\log N\text{--}\log S$  distribution towards higher or lower fluxes.

To create sensitivity maps, we calculated the number of source counts that would be required to meet our *pns* criteria ( $< 4 \times 10^{-6}$ ) for each point in the survey area. This method for generating sensitivity maps has been tested using simulated *Chandra* observations by Georgakakis et al. (2008). The 90% complete limiting flux in the 0.35–8 keV, 0.5–2 keV, and 2–8 keV energy bands are  $6.2 \times 10^{-16} \text{ erg s}^{-1} \text{ cm}^{-2}$ ,  $1.3 \times 10^{-16} \text{ erg s}^{-1} \text{ cm}^{-2}$ , and

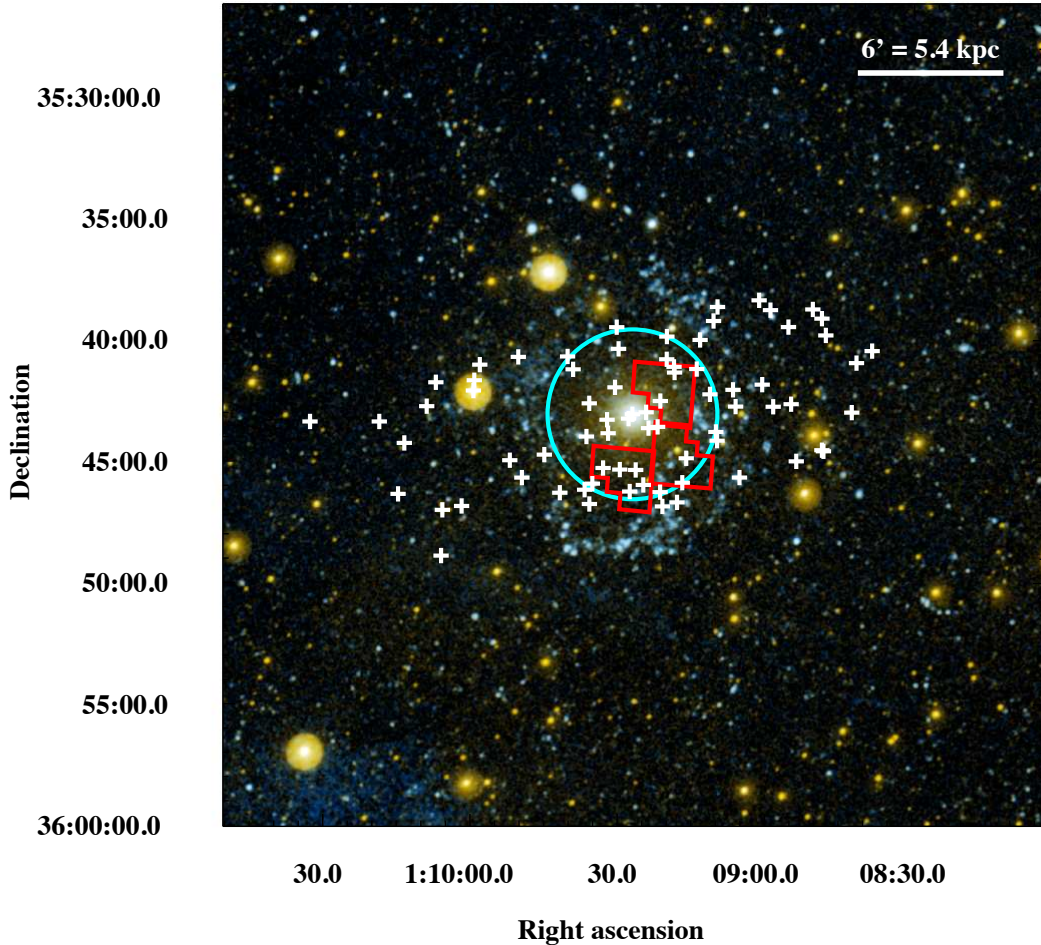


FIG. 3.— RGB rendered *GALEX* image of NGC 404. White crosses indicate the locations of the X-ray sources in the NGC 404 catalog. The optical extent of the galaxy is shown by the cyan circle, and our overlapping *HST* fields are outlined in red.

TABLE 4  
MERGED  $\log(pns)$  VALUES FOR DIFFERENT ENERGY BANDS

Source No.	$\log(pns$ [1]) (0.5-8.0 keV)	$\log(pns$ [2]) (0.5-2.0 keV)	$\log(pns$ [3]) (2.0-8.0 keV)	$\log(pns$ [4]) (0.35-8.0 keV)	$\log(pns$ [5]) (0.35-1.1 keV)	$\log(pns$ [6]) (1.1-2.6 keV)	$\log(pns$ [7]) (2.6-8.0 keV)	$\log(pns$ [8]) (0.35-2.0 keV)
(1)	(2)	(3)	(4)	(5)	(6)	(7)	(8)	(9)
1	<-10	<-10	<-10	<-10	<-10	<-10	<-10	<-10
2	<-10	<-10	<-10	<-10	-2.79	<-10	<-10	<-10
3	<-10	<-10	-4.61	<-10	-9.29	<-10	-3.78	-3.78
4	-9.40	<-10	-1.40	-9.52	-5.73	-7.64	-1.24	-1.24
5	<-10	<-10	<-10	<-10	-7.96	<-10	-6.47	-6.47

NOTE. — The (logarithmic)  $pns$  value is the Poisson probability of not being a source.  $\log(pns)$  values smaller than -10 have been replaced by <-10. All these cases are highly significant detections. Only the first five entries are shown.

$8.7 \times 10^{-16}$  erg  $s^{-1}$   $cm^{-2}$ , respectively. At the distance of NGC 404, these fluxes correspond to luminosities of  $6.3 \times 10^{35}$  erg  $s^{-1}$ ,  $1.6 \times 10^{35}$  erg  $s^{-1}$ , and  $1.0 \times 10^{36}$  lum, respectively. Table 7 summarizes the limiting fluxes for the 70%, 90%, and 95% completeness levels for our total energy range, the soft band, and the hard band. For comparison, we additionally constructed sensitivity maps using the CIAO task `lim_sens`, and found the predicted limiting fluxes to be  $\sim 30\%$  higher than found using our  $pns$  analysis.

### 3. THE X-RAY SOURCE CATALOG

The X-ray properties of individual sources, such as their temporal variability and spectral shape, can be used to constrain the physical origin of the X-ray emission. Additionally, bulk population properties (such as the radial distribution of sources) enable us to identify different X-ray populations in a statistical sense. We expect the X-ray point source population of NGC 404 to consist of LMXBs, background AGN, and foreground stars. To match each source with a likely physical origin, we use our catalog to search for time-variable sources, analyze hardness ratios (for faint sources) and perform spectral fitting (for bright sources), construct a radial source dis-

TABLE 5  
TOTAL NET COUNTS IN DIFFERENT ENERGY BANDS

Source No.	<i>net_cnts</i> [1] (0.5-8.0 keV)	<i>net_cnts</i> [2] (0.5-2.0 keV)	<i>net_cnts</i> [3] (2.0-8.0 keV)	<i>net_cnts</i> [4] (0.35-8.0 keV)	<i>net_cnts</i> [5] (0.35-1.1 keV)	<i>net_cnts</i> [6] (1.1-2.6 keV)	<i>net_cnts</i> [7] (2.6-8.0 keV)	<i>net_cnts</i> [8] (0.35-2.0 keV)
(1)	(2)	(3)	(4)	(5)	(6)	(7)	(8)	(9)
1	648.0 <sup>+27.0</sup> <sub>-26.0</sub>	442.6 <sup>+22.2</sup> <sub>-21.2</sub>	205.5 <sup>+16.1</sup> <sub>-15.0</sub>	655.3 <sup>+27.2</sup> <sub>-26.1</sub>	166.3 <sup>+14.1</sup> <sub>-13.0</sub>	341.8 <sup>+19.7</sup> <sub>-18.7</sub>	147.3 <sup>+13.9</sup> <sub>-12.8</sub>	147.3 <sup>+13.9</sup> <sub>-12.8</sub>
2	116.1 <sup>+13.0</sup> <sub>-12.0</sub>	51.6 <sup>+8.7</sup> <sub>-7.7</sub>	64.5 <sup>+10.3</sup> <sub>-9.2</sub>	116.5 <sup>+13.1</sup> <sub>-12.0</sub>	7.3 <sup>+4.4</sup> <sub>-3.3</sub>	61.7 <sup>+9.4</sup> <sub>-8.3</sub>	47.4 <sup>+9.1</sup> <sub>-8.0</sub>	47.4 <sup>+9.1</sup> <sub>-8.0</sub>
3	66.9 <sup>+10.5</sup> <sub>-9.5</sub>	47.1 <sup>+8.3</sup> <sub>-7.3</sub>	19.8 <sup>+7.2</sup> <sub>-6.1</sub>	67.4 <sup>+10.6</sup> <sub>-9.5</sub>	16.1 <sup>+5.4</sup> <sub>-4.3</sub>	35.1 <sup>+7.5</sup> <sub>-6.4</sub>	16.2 <sup>+6.6</sup> <sub>-5.5</sub>	16.2 <sup>+6.6</sup> <sub>-5.5</sub>
4	32.6 <sup>+8.2</sup> <sub>-7.1</sub>	25.3 <sup>+6.5</sup> <sub>-5.4</sub>	7.3 <sup>+5.7</sup> <sub>-4.6</sub>	33.2 <sup>+8.3</sup> <sub>-7.2</sub>	10.6 <sup>+4.7</sup> <sub>-3.6</sub>	16.4 <sup>+5.7</sup> <sub>-4.5</sub>	6.2 <sup>+5.3</sup> <sub>-4.2</sub>	6.2 <sup>+5.3</sup> <sub>-4.2</sub>
5	34.3 <sup>+7.1</sup> <sub>-6.0</sub>	19.6 <sup>+5.6</sup> <sub>-4.4</sub>	14.7 <sup>+5.1</sup> <sub>-4.0</sub>	34.2 <sup>+7.1</sup> <sub>-6.0</sub>	6.8 <sup>+3.8</sup> <sub>-2.6</sub>	18.6 <sup>+5.4</sup> <sub>-4.3</sub>	8.9 <sup>+4.3</sup> <sub>-3.1</sub>	8.9 <sup>+4.3</sup> <sub>-3.1</sub>

NOTE. — Only the first five entries are shown.

TABLE 6  
PHOTON FLUX (PHOTONS CM<sup>-2</sup> S<sup>-1</sup>) IN DIFFERENT ENERGY BANDS

Source No.	$\log(flux)$ [1] (0.5-8.0 keV)	$\log(flux)$ [2] (0.5-2.0 keV)	$\log(flux)$ [3] (2.0-8.0 keV)	$\log(flux)$ [4] (0.35-8.0 keV)	$\log(flux)$ [5] (0.35-1.1 keV)	$\log(flux)$ [6] (1.1-2.6 keV)	$\log(flux)$ [7] (2.6-8.0 keV)	$\log(flux)$ [8] (0.35-2.0 keV)
(1)	(2)	(3)	(4)	(5)	(6)	(7)	(8)	(9)
1	-4.38	-4.72	-4.82	-4.36	-4.77	-4.87	-4.95	-4.95
2	-5.23	-5.76	-5.43	-5.22	-6.23	-5.72	-5.55	-5.55
3	-5.46	-5.78	-5.94	-5.45	-5.85	-5.95	-6.01	-6.01
4	-5.79	-6.07	-6.39	-5.78	-6.08	-6.30	-6.45	-6.45
5	-5.26	-5.66	-5.58	-5.25	-5.66	-5.74	-5.78	-5.78

NOTE. — Only the first five entries are shown.

TABLE 7  
LIMITING UNABSORBED FLUXES FOR THE COMBINED NGC 404 OBSERVATIONS<sup>a</sup>

Energy Band (keV)	70% (10 <sup>-16</sup> erg s <sup>-1</sup> cm <sup>-2</sup> )	90% (10 <sup>-16</sup> erg s <sup>-1</sup> cm <sup>-2</sup> )	95% (10 <sup>-16</sup> erg s <sup>-1</sup> cm <sup>-2</sup> )
(1)	(2)	(3)	(4)
0.35-8	5.0	6.2	19.8
0.5-2	0.3	1.3	4.4
2-8	2.8	8.7	27.5

NOTE. — <sup>a</sup>Limiting fluxes are estimated assuming the standard model ( $\Gamma = 1.9$ ).

tribution, and create XLFs. The addition of overlapping *HST* fields allows us to identify optical counterpart candidates.

### 3.1. Time Variable Sources

The full NGC 404 catalog was systematically searched for sources showing both significant short-term (i.e., variability that occurs on timescales less than the exposure time,  $\sim 27$  hours) and long-term variability in the 0.35-8 keV band. While rapid X-ray variability is routinely observed in both AGN and XRB systems (Vaughan et al. 2003), it is typically not observed in other sources of X-ray emission (i.e., SNRs). We used a Kolmogorov-Smirnov (K-S) test to compare the cumulative photon arrival time distribution for each X-ray source to a uniform count rate model. The K-S test returns the probability (denoted by  $\xi$ ) that both distributions were drawn from the same parent distribution. We searched for rapid variability only in Obs ID 12239, due to its significantly longer exposure time than the archival observations. We used the three separate *Chandra* observations to search for significant changes in the long-term X-ray flux of each source.

Only two sources, 1 and 72, have K-S probabilities of 0.06% and 0.09% respectively, which may be indicative of potential short-term variability. To investigate the long-term variability of each of the NGC 404 sources,

we utilize the variability threshold  $\eta$  (as in Tüllmann et al. 2011), defined as  $\eta = (flux_{\max} - flux_{\min})/\Delta flux$ , where  $flux_{\max}$  and  $flux_{\min}$  are the maximum and minimum observed fluxes of the source, respectively, and the flux error  $\Delta flux$  is calculated using the Gehrels approximation (appropriate for low count data; Gehrels 1986). We consider any sources with  $\eta \geq 3$  potentially variable. One source (#16) in NGC 404 has  $\eta \geq 5$  and is highly likely to exhibit long-term variability.

We also consider the possibility that the NGC 404 catalog may contain transient sources. We found 18 X-ray sources that were detected in at least one exposure, but were not detected in another exposure (despite the source's position being within the field of view). We use these non-detections to place an upper limit on the source flux at the time of the exposure; some of these sources are faint, and so may have been just below the detection limit of the shallower exposure without requiring a significant change in flux. However, seven X-ray sources exhibited a change in X-ray flux of at least an order of magnitude and had  $\eta \geq 3$  – we refer to these sources as candidate X-ray transients (XRTs). Both LMXBs and HMXBs are known to experience X-ray outbursts of this magnitude (Bozzo et al. 2008; Fragos et al. 2008; Paul & Naik 2011; Revnivtsev et al. 2011), and may have implications for the slope of the XLF (see § 5).

Table 8 lists the variability properties for all sources in



the NGC 404 catalog that exhibit some form of temporal variability. We include three potentially variable sources (sources 27, 49, and 57, noted with italics) which fall short of our definition of an XRT candidate by less than 10%. That is, if any of these three sources were to change either their lowest or highest observed fluxes by less than 10%, the fractional change in flux would be more than an order of magnitude (the typical flux error for an NGC 404 source is  $\sim 20\text{-}25\%$ ).

### 3.2. Radial Source Distribution

While direct, multiwavelength detection of X-ray source counterparts provides an excellent means of discriminating between sources associated with NGC 404 and background or foreground contaminants, this approach is likely to fail when classifying faint sources. As a result, the physical nature of many faint X-ray sources in our catalog will remain ambiguous. We therefore adopt an additional, statistical approach to constrain the number of sources in NGC 404.

We construct an X-ray galactocentric profile of the NGC 404 by summing number of sources detected as a function of galactocentric radius. We assign an inclination-corrected galactocentric distance to each X-ray sources assuming the galaxy center is located at  $\alpha_0 = 17^{\circ}36'25.00$ ,  $\delta_0 = +35^{\circ}71'80.56$  (Evans et al. 2010), and  $i = 11^{\circ}$  (del Río et al. 2004). The maximum radius we find for an X-ray source in our *Chandra* field is  $r = 6.1$  kpc. We divide the X-ray sources into radial bins (spaced 0.7 kpc apart) based on their distance from the center of the galaxy. We use the cumulative  $\log N\text{-}\log S$  distribution of Cappelluti et al. (2009), corrected for the decreasing *Chandra* sensitivity with increasing off-axis angle, to estimate the expected contamination by background AGN. This was done by finding the number of AGN predicted (for the flux sensitivity of our survey) for the area spanned by each radial bin. In Figure 4, we show both a histogram of our derived galactocentric distances and the number of X-ray sources per square kpc.

The majority of the NGC 404 X-ray sources have  $r \lesssim 2.5$  kpc, and the number of X-ray sources per  $\text{kpc}^2$  beyond 2.5 kpc is roughly equal to the number predicted by the AGN  $\log N\text{-}\log S$  distribution. We therefore expect the 29 X-ray sources with  $r > 2.5$  kpc to be predominantly contaminating background AGN or foreground stars, while the X-ray sources with  $r < 2.5$  kpc are expected to be a mix of contaminants and X-ray sources associated with NGC 404. This interpretation is consistent with the observed bulge effective radius ( $r_e = 0.9 \pm 0.4$  kpc) and disk scale length ( $\sim 1.9$  kpc) derived by both Baggett et al. (1998) and Williams et al. (2010).

### 3.3. Hardness Ratios

The X-ray spectrum of a source can provide a key diagnostic for separating different populations. For example, LMXBs and AGN are well-described by power laws with photon indices ranging from  $\Gamma \sim 1 - 2$ , and may show high levels of intrinsic absorption (i.e., in the case of obscured AGN). Super-soft sources (SSSs) and contaminating foreground stars will exhibit significantly softer, thermal X-ray emission with plasma temperatures of a few keV or less. However, when studying XRBs at distances of a few Mpc it is near impossible to constrain spectral

parameters to any degree of accuracy, especially for those sources with  $\lesssim 50$  counts. The majority of NGC 404 X-ray sources fall within this low-count regime, as shown in Figure 5.

Instead of directly measuring the X-ray spectral shape, we define hardness ratios (HRs; also called X-ray colors) to separate different populations. HRs measure the fraction of photons emitted by a source in three energy ranges: soft ( $S$ , 0.35-1.1 keV), medium ( $M$ , 1.1-2.6 keV), and hard ( $H$ , 2.6-8 keV). We evaluate two HRs for each source using the approach developed in Tüllmann et al. (2011) (see also Prestwich et al. 2009). Source and background counts were determined by AE in each band, and we define a “soft” color,

$$HR1 = \frac{M - S}{H + M + S}, \quad (1)$$

and a “hard” color,

$$HR2 = \frac{H - M}{H + M + S}. \quad (2)$$

We use the Bayesian Estimation of Hardness Ratios<sup>7</sup> (*BEHR*, Park et al. 2006) in a similar manner as described by Tüllmann et al. (2011) and Prestwich et al. (2009) to determine the hardness ratios of the NGC 404 X-ray sources. For low-count sources (which make up the majority of the NGC 404 point source catalog), the net counts can be negative due to fluctuations in the source and background estimates, resulting in unphysical HRs when calculated using a traditional approach. The *BEHR* code accounts for the fact that source and background counts are non-negative, ensuring that our approach produces physically allowable values of the HRs. In the high-count regime, the results of the Bayesian approach become equivalent to traditionally-computed HRs.

For each source, the inputs are source counts, background counts, the AE “backscale” parameter (which accounts for the ratio of the source and background extraction areas and efficiencies), and a factor converting from counts to photon flux (i.e., the exposure time multiplied by the mean ARF over the extraction region in the respective energy band). The “softeff” and “hardeff” parameters take into account the variations in effective area and exposure times between the different observations, especially important considering the strong differences in ACIS filter contamination between the observations utilized in this work; we set these parameters to the exposure time multiplied by the mean ARF values computed by AE in the appropriate energy band for each observation in which the source was observed.

The *BEHR* code is then run twice (once for  $S$  and  $M$ , and again for  $S$  and  $H$ ). For each energy band, we set the *BEHR* “burnin” parameter to 50,000 and the “total draws” parameter to 100,000. This provides 50,000 samples from the probability distribution for each energy band. Combining the results from the two *BEHR* runs, we obtain 50,000 samples from the probability distribution for the  $S$ ,  $M$ , and  $H$  counts. Using these distributions, we compute 50,000 values for  $HR1$  and  $HR2$  for

<sup>7</sup> <http://hea-www.harvard.edu/AstroStat/BEHR/>

TABLE 8  
TEMPORAL VARIABILITY OF NGC 404 X-RAY SOURCES

Source No.	$\xi^a$	$\eta^b$	$flux_{max}/flux_{min}^c$
(1)	(2)	(3)	(4)
1	< <b>0.01</b>	0.10	2.61
16	0.09	<b>5.21</b>	<b>25.28</b>
18	0.87	2.03	<b>14.74</b>
27	0.94	1.81	<i>9.21</i>
37	0.25	2.61	<b>10.12</b>
40	0.04	<b>3.44</b>	<b>14.74</b>
49	0.29	2.10	<i>9.46</i>
53	0.92	1.90	<b>13.78</b>
54	0.69	<b>3.02</b>	<b>23.53</b>
55	0.79	<b>4.22</b>	<b>42.64</b>
57	0.56	2.00	<i>9.19</i>
59	0.49	<b>4.96</b>	<b>23.17</b>
61	0.89	<b>3.37</b>	<b>26.60</b>
64	1.00	<b>4.65</b>	<b>42.46</b>
71	0.06	<b>4.46</b>	<b>34.79</b>
72	< <b>0.01</b>	0.11	1.13

NOTE. —

<sup>a</sup>The K-S probability of the source being constant within our *Chandra* observation Obs ID 12239 (short-term variability). Sources with K-S probabilities of  $\xi \leq 3.7 \times 10^{-3}$  are likely to show short-term variability and are shown in boldface.

<sup>b</sup> $\eta$  is the variability index defined by Tüllmann et al. (2011) and is sensitive to long-term variability. Sources with  $\eta \geq 3$  are likely to show variability between the individual *Chandra* exposures.

<sup>c</sup>Sources whose fluxes changed by more than an order of magnitude are shown in boldface; sources just short of this threshold (by less than 10%) are shown in italics.

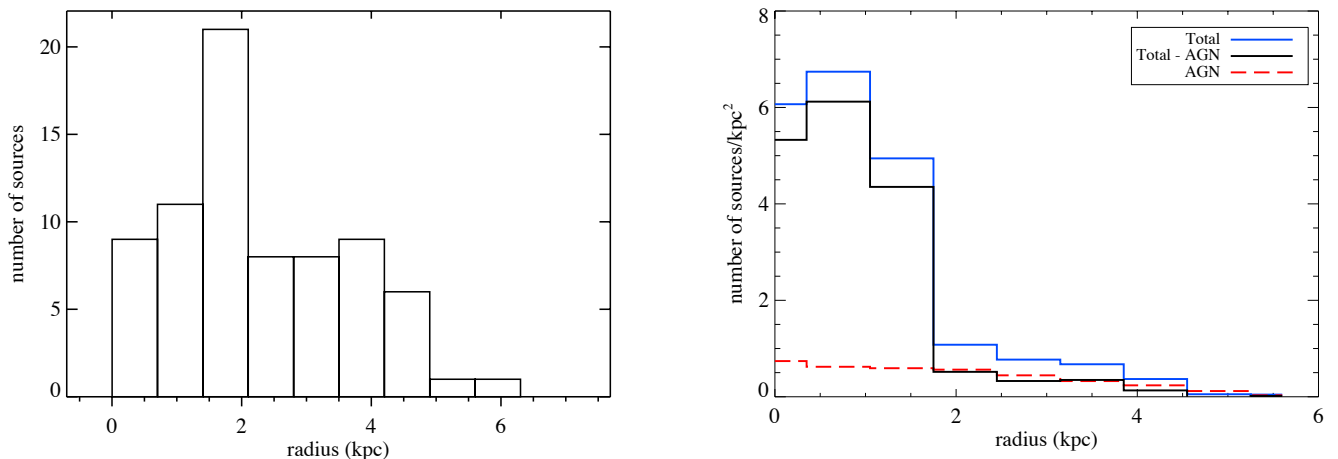


FIG. 4.— Left: histogram of galactocentric distances for the NGC 404 X-ray source catalog. Right: galactocentric source density profile of NGC 404 in the 0.35–8.0 keV band. The blue histogram shows the total number of sources per square kiloparsec. The red dashed line shows the anticipated number of background AGNs (corrected for the *Chandra* ACIS off-axis sensitivity), while the black histogram shows the expected number of sources after correcting for background AGNs.

each source. Because the difference of two Poisson distributions does not follow Poisson statistics, we do not use the error estimates directly provided by these *BEHR* runs. Instead, the HR value is defined as the mean of the distribution, and the credible interval is evaluated based on the 68.2% equal-tail estimates (i.e., 0.682/2 of the samples have values below the lower limit, and 0.682/2 of the samples have values above the upper limit).

To aid in the interpretation of our HR calculations, we use the same X-ray color-color classification scheme developed in Paper I. We define six categories of X-ray sources: ‘XRB’ (which is likely contaminated with background AGN, given their X-ray similarities to LMXBs), ‘BKG’ for likely background sources with an indetermi-

nate spectral shape, ‘ABS’ for heavily absorbed sources, ‘SNR’ (although, given the morphology and SFH of NGC 404, these sources are likely to be foreground stars or super-soft sources, and not true supernova remnants), and indeterminate ‘HARD’ and ‘SOFT’ sources. Our X-ray color-color classification scheme, along with the number of sources belonging to each category, is given in Table 9. The HRs and corresponding source classification is given in Table 10, and a plot of our HR values is shown in Figure 6. Figure 6 additionally shows the agreement between the HRs and spectral fitting (see Section 3.4) – HRs provide a useful technique for identifying highly absorbed sources, sources with thermal emission, and sources with power law-like spectra. However, HRs



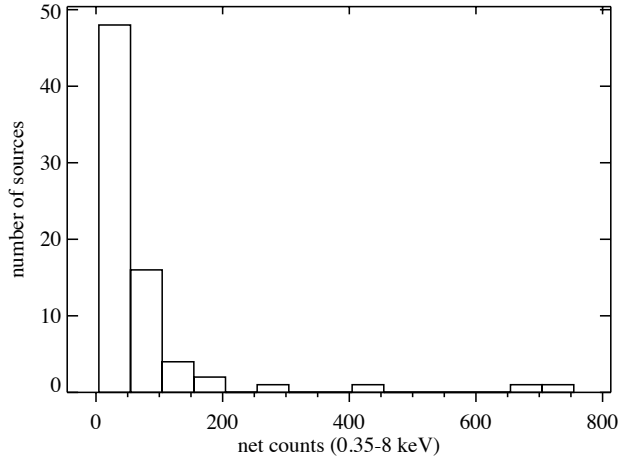


FIG. 5.— Histogram showing the NGC 404 X-ray source counts. 85% of X-ray sources in our catalog have fewer than 100 net counts.

cannot be used to separate power laws with different photon indices.

We find  $\sim 61\%$  of the NGC 404 X-ray sources fall within the ‘XRB’-like category, and  $\sim 20\%$  of sources show evidence for high levels of intrinsic absorption. Only four sources (5%) are designated as ‘SNR’-like – one of these sources (source 65) is coincident with a foreground star (see Section 3.4). Given the latitude of NGC 404 and the small area subtended by the galaxy, these are likely foreground objects not associated with NGC 404. The remaining X-ray sources are categorized as ‘HARD’ or ‘SOFT’ and are likely not associated with NGC 404.

### 3.4. X-ray Spectral Analysis

For sufficiently bright sources ( $\gtrsim 50$  counts), the X-ray spectrum of a source can be used to constrain the physical nature of the X-ray emission. Both XRBs and AGN are typically described by power laws, with photon indices ranging from  $\Gamma \sim 1 - 2$ . If the source is a likely XRB, the photon index can sometimes be used to constrain the nature of the compact object: NS primaries typically exhibit harder X-ray emission, with  $\Gamma \sim 1-1.5$ , while BHs (which lack a solid surface) often produce  $\Gamma \sim 2 - 2.5$ . Foreground stars will show significantly softer X-ray emission, and typically have their spectra fit with a thermal plasma.

Spectra were extracted by AE using the CIAO tool `dmextract`. Response products were created by AE using the CIAO tools `mkacisrmf` and `mkarf`. Due to the low number of counts found for most of the sources in our catalogs, we fit spectral models to the unbinned spectra and use  $C$ -statistics in lieu of traditional  $\chi^2$  statistics (see e.g., Cash 1979; Humphrey et al. 2009). Three sources were found have more than 200 net counts in the 0.35-8 keV band; these sources are discussed in more detail below. Detailed spectral fitting was performed for the NGC 404 central region in Binder et al. (2011).

The ungrouped spectra for 60 out of 74 sources in NGC 404 were automatically fit in AE with one of four models: a power-law model, an APEC model (Smith et al. 2001), or either a power-law or thermal model with additional absorption. The Galactic absorption was modeled with the `tbabs` model (Wilms et al. 2000) by freezing the Galactic  $N_{\text{H}}$  at  $5.13 \times 10^{20} \text{ cm}^{-2}$  (Kalberla et al. 2005).

In order to determine the best-fit model, models that predicted unreasonably high photon indices ( $\Gamma > 4$ ) or plasma temperatures ( $kT > 6.0 \text{ keV}$ ) were rejected.

Because the  $C$ -statistic cannot be directly interpreted as a goodness-of-fit, we use a different approach to select the preferred spectral model for each source. First, we used XSPEC’s `goodness` command to perform 5,000 Monte Carlo simulations for each spectral model (power law and thermal models, both with and without additional absorption). The `goodness` command simulates spectra based on the model parameters and finds the number of simulations with a fit statistic less than that found for the data. If the observed spectrum was produced by that model, the “goodness” should be  $\sim 50\%$ . For some sources, the choice of preferred spectral model was obvious: three of the spectral models yielded a `goodness` of less than  $\sim 2\%$ , while one model produced a `goodness` in the range of  $\sim 40 - 60\%$ . In the remaining cases, no obviously preferred model was found – for these sources, we chose the simple, unabsorbed power law unless the spectrum showed indications for emission features (in which case, the unabsorbed thermal model was selected). The best-fit model and parameters for sources with greater than 50 net counts are listed in Table 11. All errors represent the 90% uncertainties.

The spectra of bright sources often require multiple component models. Three X-ray sources (1, 7, and 65, excluding the NGC 404 nucleus) have more than 450 net counts, however none of these sources is likely to be associated with NGC 404. Sources 1 and 7 are likely background AGN whose spectra do not require more complex models than what is presented in Table 11.

#### 3.4.1. Source 65

Although source 65 (a likely foreground star) does not require a more complex spectral model to adequately describe its X-ray spectrum, it is interesting enough to warrant a brief discussion. Source 65 was detected in two of the observations considered here (Obs IDs 12239 and 384). The X-ray source was detected on the back-illuminated S3 chip in Obs ID 12239, while it was detected on the front-illuminated S4 detector in Obs ID 384. The differences in front and back-illuminated responses make merging the source 65 spectrum problem-

TABLE 9  
HARDNESS RATIO SOURCE CLASSIFICATION SCHEME

Classification (1)	Definition (2)	# Sources (3)
X-ray binary ('XRB')	$-0.4 < HR2 < 0.4, -0.4 < HR1 < 0.4$	45
Background source ('BKG')	$HR2 > -0.4, HR1 < -0.4$	0
Absorbed source ('ABS')	$HR1 > 0.4$	15
Supernova remnant ('SNR')	$HR2 < -0.4, HR1 < -0.4$	3
Indeterminate hard source ('HARD')	$HR2 > 0.4, -0.4 < HR1 < 0.4$	4
Indeterminate soft source ('SOFT')	$HR2 < -0.4, -0.4 < HR1 < 0.4$	7

TABLE 10  
HARDNESS RATIOS

Source No. (1)	HR1 (2)	HR2 (3)	Classification (4)
1	$0.26 \pm 0.03$	$-0.27 \pm 0.03$	XRB
2	$0.40 \pm 0.05$	$-0.04 \pm 0.08$	XRB
3	$0.24 \pm 0.08$	$-0.13 \pm 0.09$	XRB
4	$0.15 \pm 0.11$	$-0.09 \pm 0.12$	XRB
5	$0.33 \pm 0.13$	$-0.28 \pm 0.15$	XRB

NOTE. — Only the first five entries are shown.

atic; we therefore only the spectrum extracted from the 97 ks Obs ID 12239 observation (which is much higher quality than the 1.8 ks snapshot taken in Obs ID 384). Source 65 has a large off-axis angle from the nominal aimpoint of Obs ID 12239,  $\sim 6'$  8.

Source 65 (010959.34+354206.3) is the brightest X-ray source in our total NGC 404 X-ray point source catalog, excluding the NGC 404 central engine. It was detected with 708 net counts in the 0.35-8 keV band during Obs ID 12239, however the X-ray source is very soft – 97% of the counts were detected at energies below 2 keV. We therefore refine our spectral modeling by considering only the 0.35-8 keV portion of the spectrum. The best fit model is a thermal plasma APEC model, with  $kT=0.57^{+0.03}_{-0.04}$  keV ( $C/dof=106/98$ ), predicting a 0.35-8 keV flux of  $3.6 \times 10^{-14}$  erg s $^{-1}$  cm $^{-2}$ . A smoothed image of source 65 from Obs ID 12239 and the 0.35-2 keV spectrum is shown in Figure 7.

Source 65 is spatially coincident within  $\sim 0''.6$  of a high proper motion F5 star (HD 6892, Høg et al. 2000), with  $M_V \sim 8.5$  (located at a distance of  $d \sim 110$  pc). This optical magnitude implies an X-ray-to-optical flux ratio  $\log(f_X/f_V)$  of -2.9, typical of the X-ray-to-optical flux ratios reported for F stars by Agüeros et al. (2009). A UV counterpart has also been detected by GALEX, with a FUV magnitude of  $17.60 \pm 0.07$  (see §4.2). Our observations support the classification of this object as a foreground star not previously detected in X-rays.

#### 4. MULTI-WAVELENGTH COMPARISONS

##### 4.1. Optical Counterparts from *HST*

We searched for optical counterpart candidates for each of the 11 X-ray sources that was contained within one or more of the overlapping *HST* fields. The typical *Chandra* error circle for these sources was  $\sim 0''.6$ . We kept only those optical sources that met the quality cuts described in Williams et al. (2010) (i.e., sources with sufficient signal-to-noise, not flagged as unusable, meeting predetermined crowding and sharpness thresholds, etc.). The

*HST* exposures reach a typical limiting magnitude of 26 in *F814W* and 27 in *F606W*, equivalent to  $M_{814} = -1.4$  and  $M_{606} = -0.4$  (i.e., late B or early A-type main sequence stars).

Figure 8 shows *F606W*  $5'' \times 5''$  finding charts for the 11 X-ray sources with overlapping *HST* fields. Only two X-ray sources (27 and 29) were found to have optical counterpart candidates, shown in Figure 8 with arrows. The source 27 optical counterpart has  $F606W = 25.33 \pm 0.02$  and  $F606W - F814W = 1.08 \pm 0.02$ , while the optical counterpart to source 29 has  $F606W = 21.68 \pm 0.01$  and  $F606W - F814W = 2.47 \pm 0.03$ . The optical colors of both sources are consistent with a red giant branch (RGB) star or a background AGN. We estimate the X-ray-to-optical flux ratio  $\log(f_X/f_V)$  (where  $f_X$  is the 2-8 keV flux and  $f_V$  is the *F606W* flux). For source 27, we find  $\log(f_X/f_V) = 0.74$ , while source 29 has  $\log(f_X/f_V) = -2.14$ . These X-ray-to-optical flux ratios are consistent with an AGN or LMXB origin. The low number of optical counterparts, and the lack of any blue optical counterpart candidates, suggests that there are few HMXBs in NGC 404.

##### 4.2. Ultraviolet, Optical, Infrared, and Radio Counterparts

We have attempted to place additional constraints on the nature of the NGC 404 X-ray sources by examining archival multi-wavelength data. We searched for counterparts in the following point source catalogs: the *GALEX* GR6 data release (NUV, FUV), USNO-B1.0 (B, R), 2MASS All Sky (*J, H, K*), and NVSS (1.4 GHz).

UV emission can be a good tracer of young stars and background AGN; however, since the stellar populations of NGC 404 are primarily old, we expect the majority of UV-detect sources to be background AGNs. It is possible that some LMXBs in NGC 404 will exhibit detectable levels of UV emission, although their optical colors are expected to be significantly redder than that of an AGN. The optical USNO-B1.0 catalog is sensitive to Milky Way

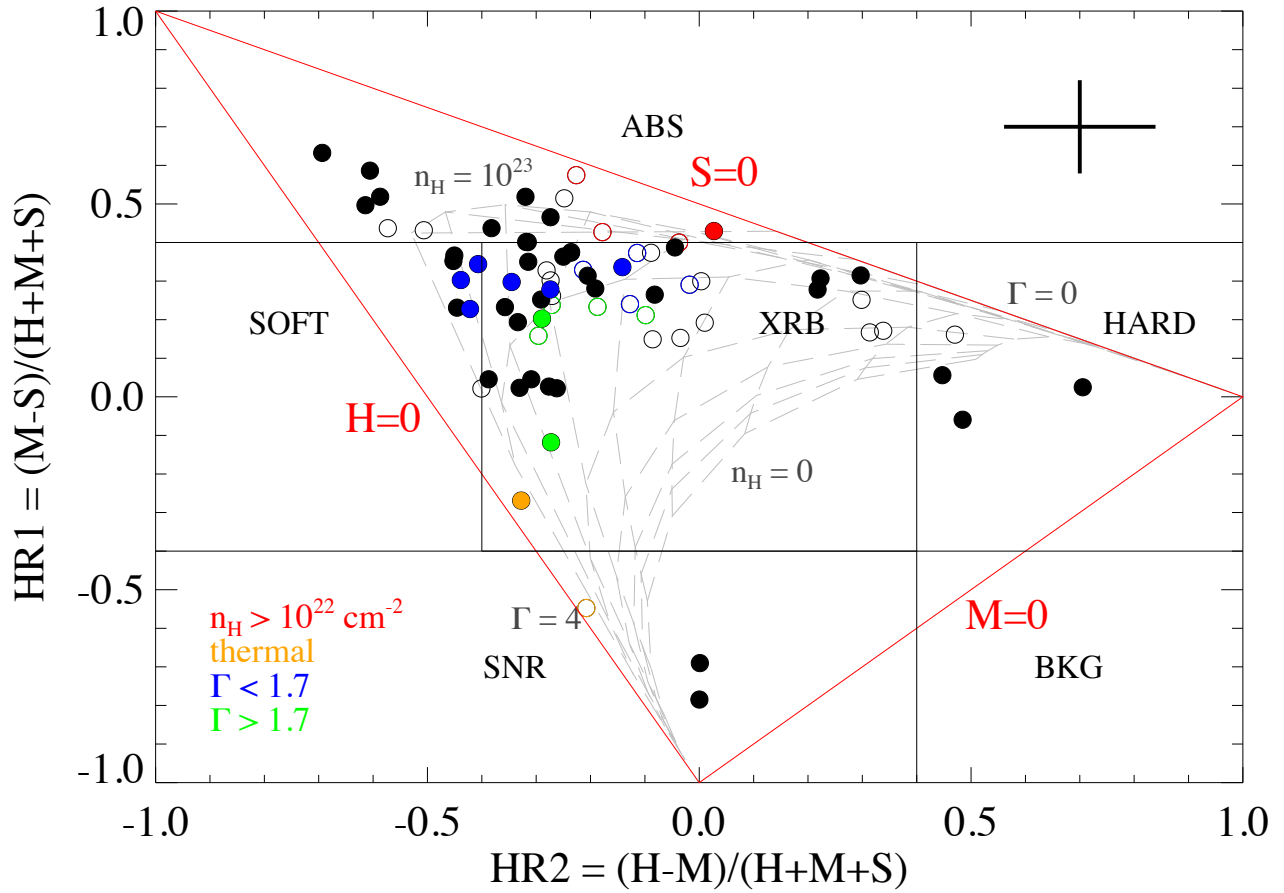


FIG. 6.— The X-ray color-color diagram. The cross in the upper-right shows the typical error size. Preliminary source classification regions are labeled. Red lines indicate the zero-count limits in the hard (‘H’), medium-hard (‘M’), and soft (‘S’) bands – HRs exterior to this red triangle are non-physical. Filled circles show sources with galactocentric radii less than  $\sim 2.5$  kpc, while open circles show sources beyond 2.5 kpc. Sources are color-coded according to their best-fit spectral model (see Section 3.4): red indicates heavy absorption, orange shows thermal sources, blue shows sources modeled as power laws with  $\Gamma < 1.7$ , and green shows sources modeled as power laws with  $\Gamma > 1.7$ . The gray lines show the X-ray colors expected for a variety of power law models (ranging from  $\Gamma = 0-4$  in steps of 0.5) with different absorbing columns (ranging from  $N_{\text{H}} = 0$  to  $10^{23}$   $\text{cm}^{-2}$ , in steps of  $2.5 \times 10^{20}$   $\text{cm}^{-2}$ ).

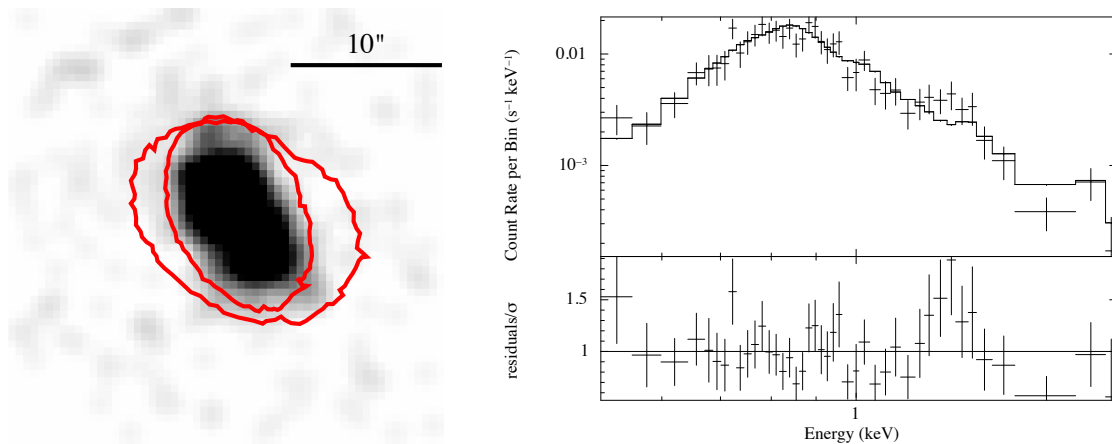


FIG. 7.— Left: *Chandra* image for source 65 (the AE source extraction regions are superimposed in red). Right: the corresponding 0.35-2 keV spectrum, binned to 20 counts per bin for display purposes only. The spectrum is best fit with a thermal plasma model, and is consistent with a stellar origin.

TABLE 11  
BEST-FIT SPECTRAL MODELS FOR SOURCES WITH MORE THAN 50 COUNTS

No.	Best-fit <sup>a</sup> Model	$N_{\text{H}}^b$ ( $10^{21}$ cm <sup>-2</sup> )	$\Gamma$	$kT$ (keV)	Norm <sup>c</sup>	$dof^d$	$C$	$f_X$ (0.5-2.0 keV) <sup>e</sup> ( $10^{-15}$ erg s <sup>-1</sup> cm <sup>-2</sup> )	$f_X$ (0.5-8.0 keV) <sup>f</sup>	goodness
(1)	(2)	(3)	(4)	(5)	(6)	(7)	(8)	(9)	(10)	(11)
1	pow	< 1.1	$1.65^{+0.12}_{-0.11}$	...	$2.02 \times 10^{-5}$	510	496	$41.1^{+1.5}_{-1.4}$	$73.4^{+5.2}_{-4.1}$	34%
2	pow	< 12	$0.6 \pm 0.3$	...	$1.48 \times 10^{-6}$	1015	943.22	$3.8^{+0.7}_{-2.9}$	$31.1^{+6.2}_{-13.6}$	88%
3	pow	< 1.1	$1.5 \pm 0.4$	...	$1.72 \times 10^{-6}$	1016	818.53	$1.6^{+0.5}_{-0.4}$	$4.8^{+1.9}_{-1.3}$	0.4%
7	pow	< 1.4	$1.8 \pm 0.1$	...	$1.18 \times 10^{-5}$	510	414	$65.6^{+7.3}_{-8.3}$	$40.7^{+4.6}_{-4.0}$	58%
11	pow	< 19	$0.8 \pm 0.4$	...	$8.14 \times 10^{-7}$	1016	964.18	$0.9^{+0.4}_{-0.3}$	$5.5^{+3.9}_{-1.7}$	12%
13	pow	< 1.9	$1.2 \pm 0.3$	...	$1.83 \times 10^{-6}$	1016	953.24	$1.8 \pm 0.4$	$7.3^{+1.7}_{-1.8}$	25%
<b>17</b>	pow	...	$1.9 \pm 0.2$	...	$5.17 \times 10^{-6}$	1016	795.63	$5.0^{+0.7}_{-0.6}$	$10.8^{+2.0}_{-1.5}$	60%
<b>20</b>	pow	...	$1.5 \pm 0.3$	...	$1.70 \times 10^{-6}$	1016	671.21	$1.6^{+0.2}_{-0.4}$	$5.0^{+1.8}_{-1.0}$	2%
<b>32</b>	apec	...	...	$0.8 \pm 0.1$	$4.56 \times 10^{-6}$	521	128.13	$8.6^{+0.3}_{-0.5}$	$9.0^{+0.2}_{-0.3}$	63%
<b>35</b>	apec	$37^{+13}_{-11}$	...	$2.8^{+3.2}_{-1.0}$	$4.77 \times 10^{-5}$	1015	829.52	$12.2^{+2.2}_{-3.6}$	$19.4^{+2.6}_{-10.1}$	95%
<b>39</b>	pow	< 1.3	$1.4 \pm 0.3$	...	$1.53 \times 10^{-6}$	1016	717.66	$1.5 \pm 0.2$	$4.8^{+1.4}_{-1.1}$	66%
<b>41<sup>g</sup></b>	pow	...	$2.1 \pm 0.2$	...	$4.56 \times 10^{-6}$	1016	657.36	$4.3^{+0.6}_{-0.3}$	$8.0^{+1.1}_{-1.0}$	82%
<b>45</b>	pow	< 1.1	$1.6 \pm 0.4$	...	$9.01 \times 10^{-7}$	1016	542.89	$0.9^{+0.3}_{-0.2}$	$2.4^{+0.9}_{-0.6}$	0.1%
<b>46</b>	pow	< 2.1	$1.4 \pm 0.2$	...	$2.73 \times 10^{-6}$	1016	823.33	$2.7^{+0.4}_{-0.5}$	$8.7^{+1.8}_{-1.5}$	33%
<b>55</b>	pow	< 3.1	$0.9 \pm 0.3$	...	$8.94 \times 10^{-7}$	1016	845.80	$0.9 \pm 0.3$	$5.5^{+1.5}_{-1.3}$	62%
58	pow	< 5.5	$1.5^{+0.4}_{-0.3}$	...	$1.10 \times 10^{-6}$	1016	762.39	$1.1 \pm 0.3$	$3.3^{+1.5}_{-0.8}$	29%
64	pow	...	$1.8 \pm 0.4$	...	$1.36 \times 10^{-6}$	1016	781.63	$1.3^{+0.4}_{-0.2}$	$3.0^{+1.2}_{-0.7}$	55%
65	apec	...	...	$0.57^{+0.03}_{-0.04}$	$4.71 \times 10^{-5}$	98	106	$40.5^{+2.3}_{-2.4}$	$41.2^{+1.5}_{-1.9}$	32%
67	pow	...	$1.2 \pm 0.5$	...	$1.11 \times 10^{-6}$	1016	923.92	$1.1 \pm 0.3$	$4.7^{+2.0}_{-1.4}$	49%
68	pow	< 4.1	$1.2 \pm 0.4$	...	$1.54 \times 10^{-6}$	1016	992.32	$1.5 \pm 0.4$	$6.4^{+3.2}_{-1.7}$	34%
70	pow	...	$1.8 \pm 0.5$	...	$2.00 \times 10^{-6}$	1016	899.26	$1.9 \pm 0.4$	$4.3^{+1.4}_{-1.4}$	41%
72	pow	...	$1.7 \pm 0.4$	...	$2.31 \times 10^{-6}$	1016	1071.92	$2.3^{+0.6}_{-0.5}$	$5.8^{+3.3}_{-1.2}$	54%
73	pow	< 9.9	$1.1 \pm 0.3$	...	$2.90 \times 10^{-6}$	1016	1108.80	$3.0^{+0.7}_{-0.5}$	$13.1^{+3.3}_{-2.7}$	72%

NOTE. — Sources with galactocentric radii less than 2.5 kpc are shown in boldface, as these sources are more likely to be associated with NGC 404.

<sup>a</sup> The best-fit model is either a **powerlaw** or **vapc** model, depending on which one has the lower  $C/dof$ .

<sup>b</sup> Intrinsic source absorption, if beyond the Galactic column was required.

<sup>c</sup> Normalization constant of the fit, in units of photons keV<sup>-1</sup> cm<sup>-2</sup> s<sup>-1</sup> and cm<sup>-5</sup>.

<sup>d</sup> Degrees of freedom.

<sup>e,f</sup> Unabsorbed X-ray fluxes.

<sup>g</sup> The NGC 404 central engine; see Binder et al. (2011).

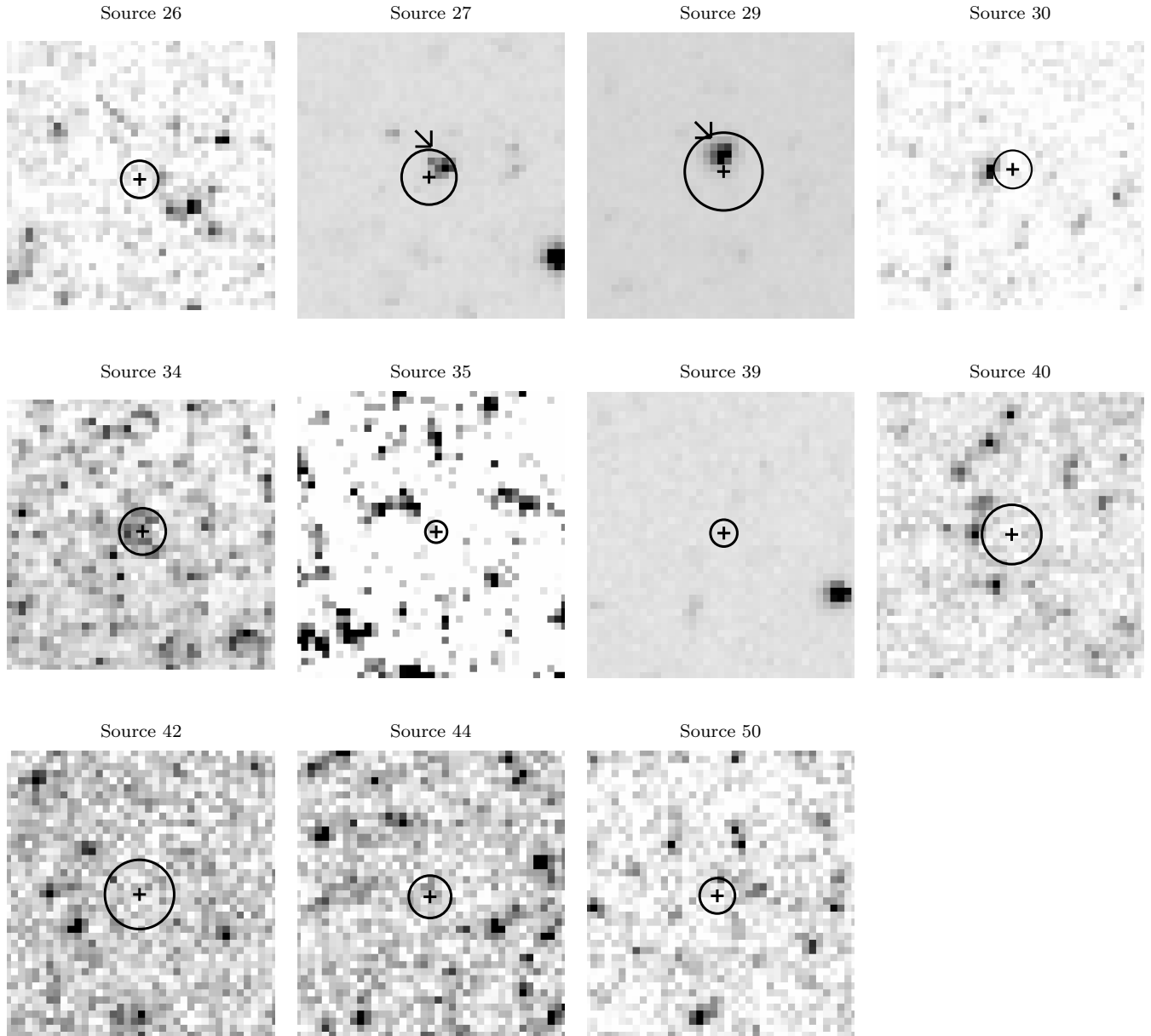


FIG. 8.— *HST* F606W postage stamps. Each square is  $5'' \times 5''$ . The black cross shows the *Chandra* X-ray source position, and the circle denotes the error circle. Optical counterpart candidates are noted with an arrow. Sources 26, 34, 40, and 42 are XRB candidates.

stars, compact clusters, and AGN. The infrared data are also sensitive to Milky Way stars, red giants, associations of older stars located in NGC 404, and background galaxies, while radio emission is indicative of radio-loud background AGN.

Table 12 summarizes the multi-wavelength observations available for each of the 31 X-ray sources with at least one multi-wavelength detection. Ten of these sources have counterpart detections in multiple wavelengths.

#### 4.3. Source Classification

We combine all of the X-ray and multi-wavelength data available for each source to determine a likely source classification. The first indicator we consider is the source’s galactocentric radius; as discussed in Section 3.2, we expect sources with  $d > 2.5$  kpc to be dominated by

contaminants (background AGN and foreground stars), while sources with  $d < 2.5$  kpc will represent a mix of sources associated with NGC 404 and those that are not. We next take into account the shape of a source’s X-ray spectrum using our derived hardness ratios (for faint sources) and X-ray spectral fitting (for sufficiently bright sources). In cases where the spectral fits and hardness ratios conflicted, we only consider the spectral fit. This occurred for only three sources (20, 32, and 45), and in all cases the sources could be described, within the uncertainties, by multiple HR classifications (i.e., source 20 is classified as ‘SOFT’ but the HR uncertainties may also place it within the ‘XRB’ category). Finally, we consider the detection of a multi-wavelength counterpart.

Sources with  $d > 2.5$  kpc and hardness ratios ‘XRB,’ ‘HARD,’ ‘BKG,’ ‘ABS,’ or with an X-ray spectrum best fit by a power law are classified as AGNs. Those sources





with additional UV or radio detections are highly likely to be background AGNs. X-ray sources with  $d > 2.5$  kpc and ‘SOFT,’ ‘SNR,’ or thermal spectra are classified as foreground stars (FSs), while softer/thermal sources with  $d < 2.5$  kpc are potentially super-soft sources (SSSs) and may be associated with NGC 404. We feel especially confident that softer sources with an IR detection in 2MASS are indeed FSs. Sources with  $d < 2.5$  kpc with ‘XRB’ hardness ratios or a power law spectrum are classified as XRBs.

Again, ‘SOFT’ and ‘SNR’ sources are classified as FSs, and sources with harder spectra are classified as AGNs. Table 13 lists our final source classifications.

We find 21 candidate XRBs, 46 likely background AGN, 4 candidates SSSs, and 2 likely FSs (plus the NGC 404 central engine). Six sources have been tentatively labeled as ‘AGN?’ but have at least one source property (for example,  $d < 2.5$  kpc) that makes them a potential XRB candidate. Given the Cappelluti et al. (2009) AGN  $\log N$ - $\log S$  distribution, we expect  $\sim 37-40$  X-ray sources to be background AGN; it is therefore likely that at least some of these six AGN candidates are in fact associated with NGC 404. We find no obvious HMXB candidates in our X-ray source catalog.

#### 4.4. Comparison to Other X-ray Source Populations

While HMXBs are expected to trace the SFR, LMXBs have been shown to correlate with the stellar mass of the host galaxy. We estimate the number ratio of LMXBs to HMXBs in NGC 404 (Gilfanov 2004) assuming a stellar mass of NGC 404 of  $6.9 \times 10^8 M_\odot$  (Thilker et al. 2010); LMXBs are expected to outnumber HMXBs by a factor of 4/10/18 at luminosities greater than  $10^{35}/10^{36}/10^{37}$  erg s $^{-1}$ . It is therefore possible that 1-2 of the X-ray sources in our catalog are HMXBs associated with NGC 404. Although we do not observe a high mass optical counterpart to an X-ray source, we note that less than 15% of the X-ray sources detected by *Chandra* have overlapping *HST* coverage.

The number of X-ray sources normalized by stellar mass was investigated by Gilfanov (2004) for both early and late type galaxies. The galaxies included in the Gilfanov (2004) sample all have stellar masses greater than a few  $10^{10} M_\odot$ —more than two orders of magnitude greater than NGC 404. We therefore test whether NGC 404 follows the same scaling relations between number of LMXBs and stellar mass as its more massive counterparts. We note that the Gilfanov (2004) work relied on X-ray source catalogs compiled from the literature; the original publications used different (broad) energy bands, assumed different spectral models for converting between count rates to energy fluxes, and employed different source detection strategies. However, it was anticipated that such differences contributed uncertainties of only  $\sim 20$ -30%. We assume the 0.35-8 keV energy flux and our standard model for all following analysis.

The Gilfanov (2004) work evaluated the number of luminous X-ray sources per unit stellar mass of the host galaxy ( $N_X/M_*$ ) found in late-type galaxies to the populations of early type galaxies (see their Table 5), although no significant difference was found between earlier- and later-type galaxies. The average number of X-ray sources more luminous than  $10^{37}$  erg s $^{-1}$  per  $10^{11} M_\odot$  stellar

mass of the host galaxy was found to be  $166.3 \pm 20.5$ . We do not find any of the NGC 404 XRB candidates to have a 0.35-8 keV luminosity above  $10^{37}$  erg s $^{-1}$ . To find an upper limit on the number of XRBs in NGC 404, we employ a similar strategy as described in Section 5 for our XLF fitting. We randomly add 10 sources from our list of background AGNs and find the number of sources above  $10^{37}$  erg s $^{-1}$ , as well as their collective luminosity. This was done 500 times. On average,  $2.2 \pm 1.3$  sources have a luminosity above  $10^{37}$  erg s $^{-1}$  with a collective luminosity of  $\sim 2.6 \times 10^{37}$  erg s $^{-1}$ . We therefore estimate the number of XRBs more luminous than  $10^{37}$  erg s $^{-1}$  in NGC 404 to be  $< 3.5$ .

Assuming NGC 404 hosts  $< 3.5$  X-ray sources above  $10^{37}$  erg s $^{-1}$ , and using the same units as Gilfanov (2004), we find  $N_X/M_*$  for NGC 404 is  $< 51$  sources per  $10^{10} M_\odot$ , more than  $5\sigma$  below the average found for more massive galaxies. Similarly, we compare the collective luminosity of sources above  $10^{37}$  erg s $^{-1}$  per unit stellar mass of the host galaxy ( $L_X/M_*$ ) of NGC 404 to the more massive galaxies considered in Gilfanov (2004). The sample average from Gilfanov (2004) was  $0.83 \pm 0.08$ , where  $L_X$  is in units of  $10^{40}$  erg s $^{-1}$  and  $M_*$  is in units of  $10^{11} M_\odot$ . In these units, we find an upper limit on  $L_X/M_*$  for NGC 404 of 0.38. Although this result is again more than  $5\sigma$  below the average for all galaxies, the  $L_X/M_*$  values show considerably more scatter for Gilfanov (2004) sample. Figure 9 shows both  $N_X/M_*$  and  $L_X/M_*$  as a function of stellar mass for the Gilfanov (2004) sample and NGC 404.

Although there is large amount of scatter among the galaxies considered in Gilfanov (2004), the upper limits on the number of XRBs and the collective luminosity of XRBs per stellar mass found for NGC 404 is low. No obvious trends in these quantities with stellar mass are observed in Figure 9, so it is unclear whether the lower stellar mass of NGC 404 is responsible for this difference. Instead, the relatively recent increase in SFR experienced by NGC 404 may have produced a population of low-luminosity LMXBs powered by MS donor stars which is currently dominating the X-ray emission from XRBs. Future work will be required to understand whether this difference in collective XRB luminosity is common for dwarf galaxies, or if NGC 404 is an outlier.

## 5. THE X-RAY LUMINOSITY FUNCTION

Numerous studies have shown a correlation between the shape of the XLF for a given X-ray source population and the SFH of the host galaxy (Kilgard et al. 2002; Grimm et al. 2003; Gilfanov 2004; Eracleous et al. 2006; Fabbiano 2006). We provided a direct observational test of these correlations for young stellar populations in Paper I, where HMXBs were the dominant source of X-ray emission. We now aim to test the XLF slope-age correlation for the older stellar populations found in NGC 404, where LMXBs are expected to be the prominent source of X-rays.

For a survey covering a total geometric area  $A$ , the cumulative number of sources  $N(> S)$  can be evaluated by summing over all sources with fluxes exceeding  $S$ , weighted by the survey area,  $A(S)$ , over which a source with flux  $S$  could have been detected:

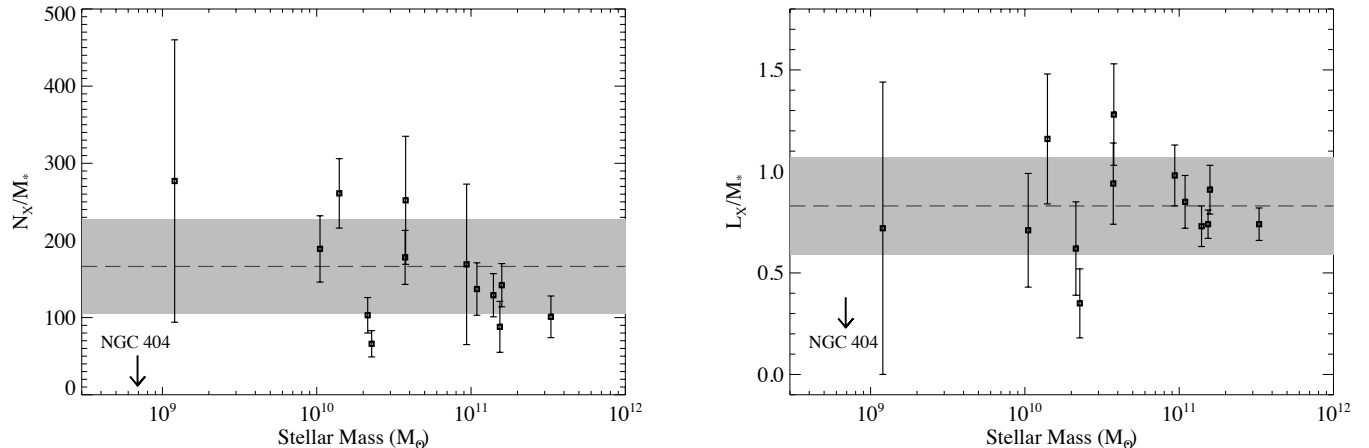


FIG. 9.— The left panel shows the number of XRBs more luminous than  $10^{37}$  erg  $s^{-1}$  per unit stellar mass of the host galaxy (in units of  $10^{11} M_{\odot}$ ), while the right panel shows the collective luminosity per stellar mass of these XRBs. In both panels, squares show the Gilfanov (2004) sample of galaxies, while NGC 404 is shown as an upper limit. The horizontal dashed lines show the average value derived from the Gilfanov (2004) sample, and the shaded region shows the  $3\sigma$  uncertainty.

$$N(> S) = \sum_{i, S_i > S} \frac{1}{A(S_i)}. \quad (3)$$

Here,  $S$  is the energy flux in units of erg  $s^{-1} \text{ cm}^{-2}$ , and  $A(S)$  survey area over which a source with flux  $S$  could have been detected;  $N(> S)$  therefore has units of sources  $\text{deg}^{-2}$ . The  $A(S)$  factor accounts for the survey completeness for sources distributed uniformly over the survey area. Although we note that sources associated with NGC 404 may not be uniformly distributed, the radial source distributions from § 3.2 did not reveal any major features in the source distributions, so uncertainties in the completeness over the survey area are likely to be small (less than  $\sim 10\%$ ). As a practical matter, we terminate the low flux end of the distribution at the 90% completeness luminosity of each energy band considered (a few  $10^{35}$  erg  $s^{-1}$ ). The sensitivity maps described above allow the area function,  $A(S)$ , to be evaluated by summing the sensitivity map over the regions where a source with flux  $S$  would be detectable. If  $N(> S)$  is given, the differential  $\log N$ - $\log S$  distribution can be computed:

$$N(S)\Delta S = \frac{N(> [S + \Delta S]) - N(> S)}{\Delta S}. \quad (4)$$

We calculate the cumulative  $\log N$ - $\log S$  distributions for all X-ray sources in the NGC 404 catalog in the soft (0.5-2 keV) and hard (2-8 keV) bands. Using our X-ray source classifications from Table 13, we then construct XLFs for those sources designated XRBs, AGNs, and SSSs. We note that the uncertainties in our X-ray source classification scheme will dominate the errors in our  $\log N$ - $\log S$  fits (discussed more below). The cumulative  $\log N$ - $\log S$  distributions for the different source categories are shown in Figure 10.

The two most significant sources of uncertainty in the XRB  $\log N$ - $\log S$  distributions are the uncertainty in the survey area over which a source could be detected (the  $A(S)$ ) and possible misclassifications of XRBs. For ex-

ample, based on our survey area and flux range, the Cappelluti et al. (2009)  $\log N$ - $\log S$  distribution of AGN predicts  $\sim 37$ -40 X-ray sources detected in the NGC 404 catalog are background AGN, implying  $\sim 34$  X-ray sources should be XRBs. However, we only classify 21 sources as XRB candidates. This discrepancy is the result of the difficulty in separating LMXBs from AGNs, which both exhibit similar X-ray and optical properties. Without further observations (for example, using the angular resolution of *HST* to resolve the disks of background galaxies), it can be nearly impossible to differentiate between LMXBs and background AGNs. Despite these uncertainties, we note that the hard  $\log N$ - $\log S$  distribution of the AGN candidates shows a break near  $10^{-14}$  erg  $s^{-1} \text{ cm}^{-2}$ , broadly consistent with the AGN  $\log N$ - $\log S$  found by both Cappelluti et al. (2009) the *Chandra* Deep Field North survey (Luo et al. 2008).

Both the differential and cumulative XRB  $\log N$ - $\log S$  distributions in the soft and hard bands are modeled as power laws with the form  $N = KS^{-\alpha}$ , where  $\alpha$  is the power law index and  $K$  is a normalization constant, using the IDL routine `mpfitfun`. The fitting is performed using only the portion of the  $\log N$ - $\log S$  distribution above the 90% limiting luminosity. These distributions, along with the best-fit models, are shown in Figure 11. The soft 0.5-2 keV distributions have a best-fit differential power law index of  $0.80 \pm 0.14$  ( $\chi^2/dof = 70.3/15$ ) and a cumulative power law index of  $1.86 \pm 0.09$  ( $\chi^2/dof = 57.8/15$ ). The hard, 2-8 keV distributions have differential and cumulative power law indices of  $0.35 \pm 0.05$  ( $\chi^2/dof = 17.7/14$ ) and  $1.09 \pm 0.03$  ( $\chi^2/dof = 88.6/14$ ), respectively.

To evaluate the effects of the AGN/LMXB classification ambiguity on our XRB  $\log N$ - $\log S$  distributions, we randomly select 10 X-ray sources classified as AGNs and add them to our list of XRB candidates. We then re-computed the  $\log N$ - $\log S$  distributions in both the soft and hard band. This was done 500 times, resulting in 500  $\log N$ - $\log S$  distributions for each of the energy bands considered. Using these new  $\log N$ - $\log S$  distributions, we checked whether (1) a simple power-law model pro-

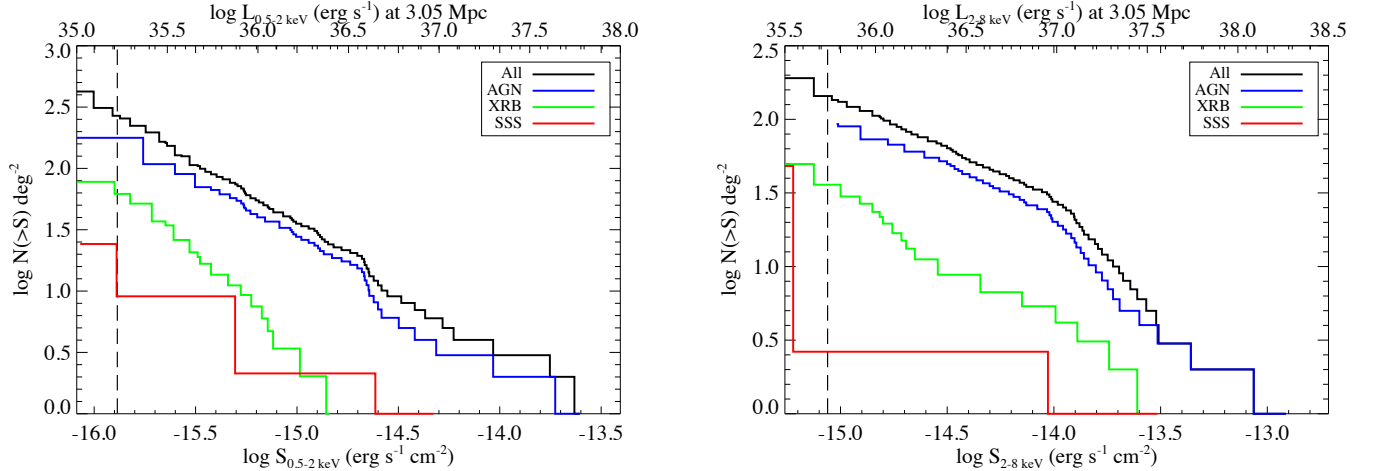


FIG. 10.— The cumulative 0.5-2 keV (left) and 2-8 keV (right) X-ray  $\log N$ - $\log S$  distributions for NGC 404. The dashed line indicates the 90% completeness limit for each energy band. The  $\log N$ - $\log S$  distribution for the total X-ray source catalog is shown in black. The  $\log N$ - $\log S$  distributions evaluated for our AGN candidates, XRB candidates, and SSS candidates are shown in blue, green, and red, respectively.

vided an acceptable fit to the new data and (2) if the slope of the best-fit power law model changed when additional sources were included. A single power-law model provided a statistically acceptable fit a clear majority of the 0.5-2 keV  $\log N$ - $\log S$  distributions. Of the 500 runs, less than  $\sim 8\%$  of the resulting distributions yielded  $\chi^2/dof > 1.5$ , although the typical power law index flattened significantly to  $1.19 \pm 0.28$  (see Figure 12a). While none of the XRB candidates have a 0.5-2 keV flux above  $\sim 1.6 \times 10^{-15} \text{ erg s}^{-1} \text{ cm}^{-2}$ , several AGN candidates do; therefore, misclassifying even a small number of relatively bright LMXBs as AGNs dramatically influences the slope of the soft XLF.

When the 500 hard  $\log N$ - $\log S$  distributions were modeled with single and broken power laws,  $\sim 52\%$  of the new 2-8 keV  $\log N$ - $\log S$  distributions were not well-described by the simple power law model. A broken power law was required to obtain a statistically acceptable fit, with an average break flux of  $(1.1 \pm 0.3) \times 10^{-14} \text{ erg s}^{-1} \text{ cm}^{-2}$ , corresponding to a luminosity of  $(1.2 \pm 0.4) \times 10^{37} \text{ erg s}^{-1}$  at the distance of NGC 404. The typical faint-end slope was  $0.78 \pm 0.06$  and the typical bright-end slope was  $1.50 \pm 0.18$ . Similar breaks in the LMXB XLF have been reported for other external galaxies (see e.g., Primini et al. 1993; Gilfanov 2004; Voss & Gilfanov 2006, 2007; Voss et al. 2009). While we do not observe an obvious break in the hard  $\log N$ - $\log S$  distribution of NGC 404 sources classified as XRBs, even a small number of misclassified AGN could have a significant effect on the shape of the XLF.

### 5.1. Comparison to Other XRB Populations

The shape of the hard XLF is consistent with observations of LMXB populations (over similar energy ranges) in external galaxies (Primini et al. 1993; Gilfanov 2004; Voss & Gilfanov 2006, 2007; Voss et al. 2009) and the Milky Way (Grimm et al. 2002; Gilfanov 2004). We additionally note that nearly all elliptical galaxies used to construct XLFs in the literature have a larger stellar mass, by an order of magnitude or more, than the dwarf galaxy NGC 404; e.g., Cen A (Wernli et al. 2002),

NGC 1407 (Kim & Fabbiano 2004; Trentham et al. 2006), NGC 4372 (Napolitano et al. 2011). No obvious correlation between XLF slope and stellar mass of the host galaxy is observed.

Several explanations for the  $\sim 10^{37} \text{ erg s}^{-1}$  break in the XLF of LMXBs have been proposed. One particularly attractive explanation involves the nature of the donor companion star: for a persistent, sub-Eddington LMXB, the accretion luminosity  $L_X$  is directly proportional to the mass transfer rate  $\dot{m}$  from the secondary star – thus, mass transfer in a LMXB can be driven by either the loss of orbital angular momentum (Paczynski & Sienkiewicz 1981; Verbunt & Zwaan 1981) or the increasing radius of the donor due to nuclear evolution (Taam 1983; Ritter 1999). Recently, Revnivtsev et al. (2011) showed that LMXB systems with X-ray luminosities below  $\sim 2 \times 10^{37} \text{ erg s}^{-1}$  have unevolved, main sequence (MS) secondary companions, while systems exhibiting higher X-ray luminosities possess predominantly giant donors. Mass transfer from a giant companion greatly shortens the lifetime of the binary, thus steepening the XLF at the high-luminosity end. The boundary between MS and giant companions has also been found in numerical simulations of LMXB populations by Fragos et al. (2008) and Kim et al. (2009).

Unlike its more massive counterparts, NGC 404 experienced a period of enhanced star formation  $\sim 0.5 \text{ Gyr}$  ago (Williams et al. 2010). Although massive stars would have expired after  $\sim 100 \text{ Myrs}$ , F and G-type stars formed during this epoch would still be on the MS. This scenario additionally explains the lack of optical counterparts observed with the overlapping *HST* exposures – at a distance of 3.05 Mpc, A-type stars and later would fall below our optical detection limits. Further FUV observations performed by *GALEX* suggest that NGC 404 may host a small number of stars as young as  $\sim 160 \text{ Myr}$  old. Stellar population studies have shown that dwarf ellipticals exhibit, on average, younger stellar ages compared to their massive counterparts (Michielsen et al. 2008) – the same may be true for the X-ray populations of dwarf ellipticals. It is therefore plausible that NGC 404 hosts a population

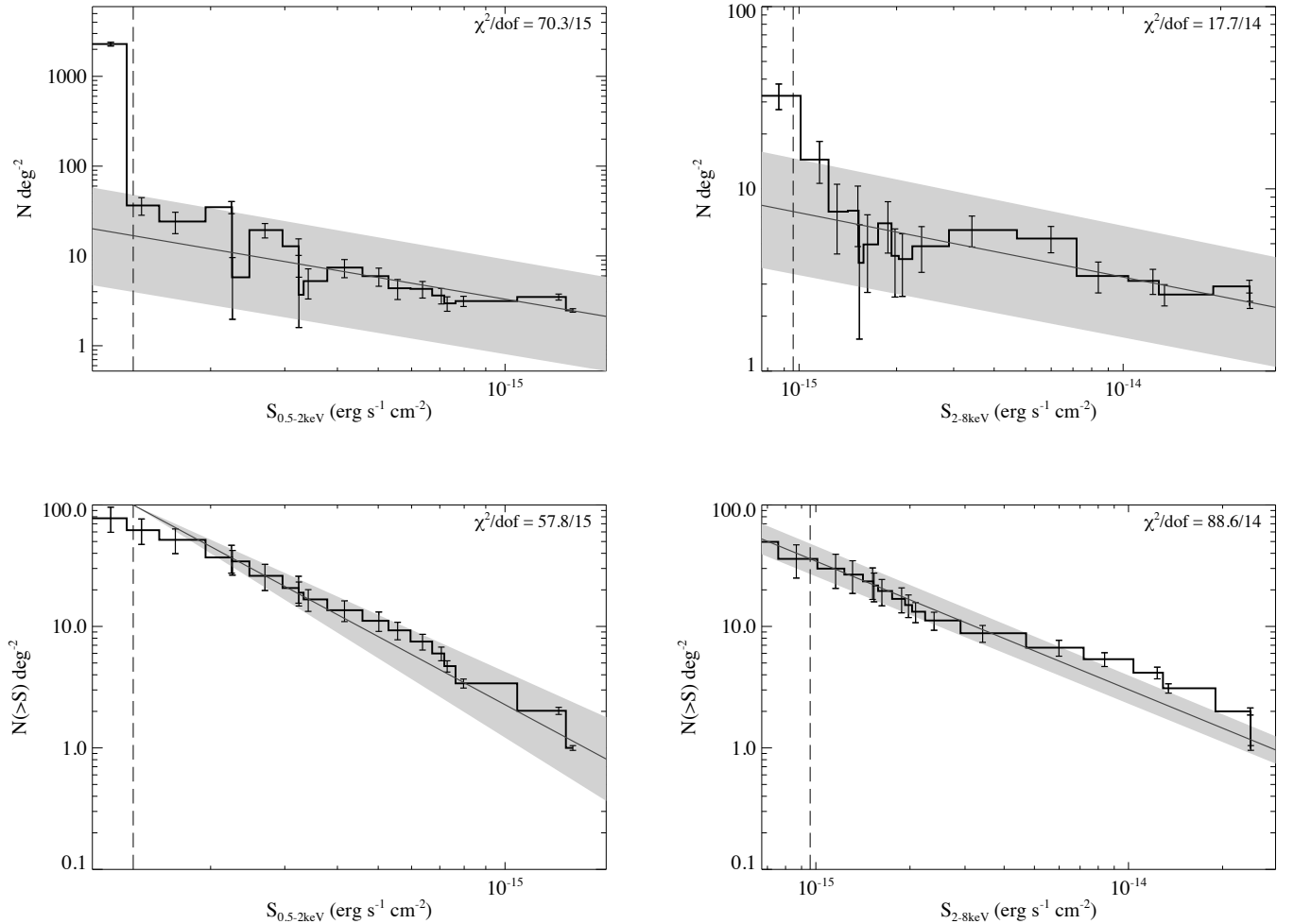


FIG. 11.— The top row shows the differential  $\log N$ - $\log S$  distributions of the NGC 404 XRB candidates in the 0.5-2 keV (left) and 2-8 keV (right) bands, while the bottom row shows the cumulative  $\log N$ - $\log S$  distributions (again, the soft band is on the left and the hard band on the right). In all four panels, the best-fit power law model is superimposed, with the gray shaded region showing the  $1\sigma$  uncertainty in the fit. The vertical dashed line shows the 90% limiting flux.

of LMXBs powered by MS donors, not typically found in more massive ellipticals.

The recent ( $<400$  Myr) star formation rate (SFR) density of NGC 404 was estimated using *HST* observations to be  $\sim 2 \times 10^{-4} M_{\odot} \text{ yr}^{-1} \text{ kpc}^{-2}$  (Williams et al. 2010). No radial trends in the SFR out to  $\sim 5$  kpc were observed, implying a typical SFR of  $\sim 0.005 M_{\odot} \text{ yr}^{-1}$ . Thilker et al. (2010) additionally estimated the SFR in the H I ring at 1.6-6.4 kpc to be  $0.0025 M_{\odot} \text{ yr}^{-1}$ . X-ray emission from HMXBs has been shown to trace recent star formation of the host galaxy (Grimm et al. 2003), and the HMXBs identified in Paper I were successfully used to confirm the SFR of NGC 300. However, the recent SFR of NGC 404 is a factor of  $\sim 70$  lower than is observed in NGC 300. Using the estimated 2-10 keV luminosity of all of our XRB candidates, we place an upper limit on the NGC 404 SFR of  $0.01 M_{\odot} \text{ yr}^{-1}$ , a factor of  $\sim 2$ -4 larger than the observed rate. This represents one of the first attempts to use X-ray emission to constrain the SFR of an early-type dwarf galaxy.

## 6. SUMMARY AND CONCLUSIONS

We have presented X-ray point source catalogs for a new, deep *Chandra* observation of NGC 404 as part of the CLVS. A total of 74 sources were detected in NGC 404 down to a 90% limiting 0.35-8 keV luminosity of  $\sim 6 \times 10^{35} \text{ erg s}^{-1}$  if we adopt our standard power law model with  $\Gamma = 1.9$ . We evaluated hardness ratios for each X-ray source, performed spectral fitting for those sources with greater than 50 counts, and presented the radial source distribution of the NGC 404 X-ray sources.

We searched for optical counterpart candidates using *HST*; 11 X-ray sources were observed in an overlapping *HST* field, and only two X-ray sources have candidate optical counterparts. We additionally cross-correlated the X-ray source catalog with *GALEX* point source catalog, USNO-B1.0, the 2MASS All-Sky Survey, and the NVSS all-sky radio survey; 31 X-ray sources have at least one multi-wavelength counterpart detected. By combining the results of our X-ray analysis with public multi-wavelength data, we assigned each X-ray source a likely classification (XRB, background AGN, or foreground star).

The differential and cumulative  $\log N$ - $\log S$  distribu-

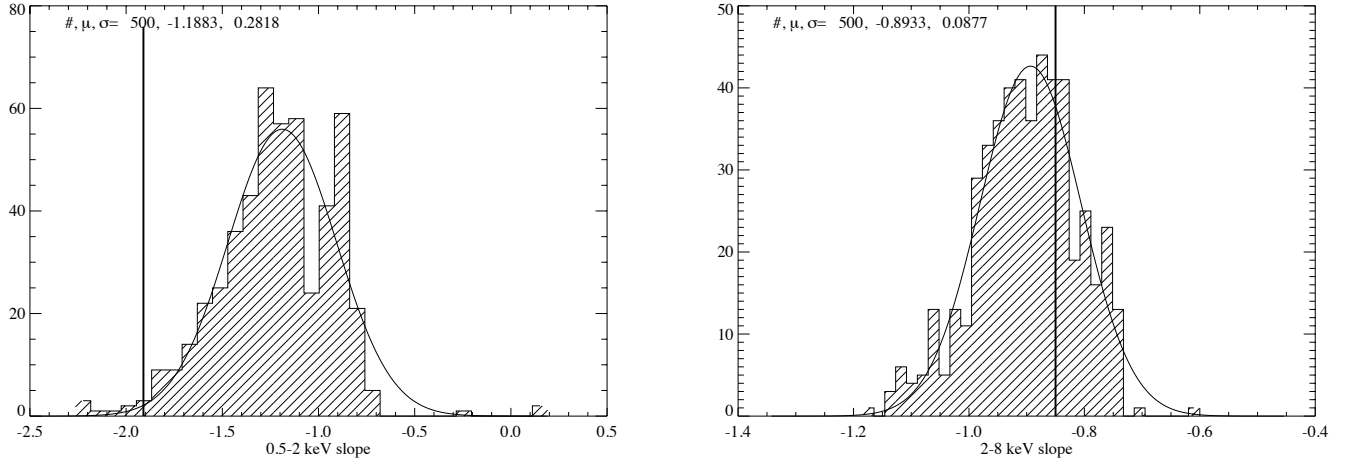


FIG. 12.— The distribution of XLF power law slopes for the soft band (left) and the hard band (right) when ten random AGN are included in the XRB  $\log N$ - $\log S$  distribution. A Gaussian was fit to each of the histogram distributions of best-fit slopes. The thick vertical lines show the best-fit  $\log N$ - $\log S$  slopes without the the randomly added AGN. The text at the top of each plot shows the number of runs (500 for both energy bands), the mean value of the slopes, and the standard deviation.

tions were presented for both the 0.5-2 keV and 2-8 keV bands. While we do not observe an obvious break in the hard  $\log N$ - $\log S$  distribution of NGC 404 sources classified as XRBs (as has been observed in other galaxies with X-ray populations dominated by LMXBs), even a small number of misclassified AGN could have a significant effect on the shape of the XLF. We derive the expected ratio of LMXBs to HMXBs in NGC 404. We expect LMXBs to outnumber HMXBs by 4/10/18 at luminosities greater than  $10^{35}/10^{36}/10^{37}$  erg s $^{-1}$ . Additionally, the NGC 404 hosts fewer luminous ( $> 10^{37}$  erg s $^{-1}$ ) XRBs per stellar mass than its more massive counterparts. The prevalence of low-luminosity XRBs in NGC 404 may be explained by a population of young LMXBs powered by MS companions; unlike its more massive counterparts, NGC 404 is known to have experienced an epoch of enhanced star formation activity  $\sim 0.5$  Gyr ago. F and G-type stars formed during this epoch

would still be on the MS, and would be below our *HST* observational detection limits – thereby also explaining the relative lack of optical counterparts found.

We thank the anonymous referee for numerous detailed and thoughtful comments and suggestions. We also thank the editor, Eric Feigelson, for helpful comments. Support for this work was provided by the National Aeronautics and Space Administration through Chandra Award Number G01-12118X issued by the Chandra X-ray Observatory Center, which is operated by the Smithsonian Astrophysical Observatory for and on behalf of the National Aeronautics Space Administration under contract NAS8-03060. T.J.G acknowledges support under NASA contract NAS8-03060. This research has made use of the NASA/IPAC Extragalactic Database (NED) which is operated by the Jet Propulsion Laboratory, California Institute of Technology, under contract with the National Aeronautics and Space Administration.

#### REFERENCES

08. 1  
 Agüeros, M. A., et al. 2009, ApJS, 181, 444  
 Baggett, W. E., Baggett, S. M., & Anderson, K. S. J. 1998, AJ, 116, 1626  
 Belczynski, K., Kalogera, V., Zezas, A., & Fabbiano, G. 2004, ApJ, 601, L147  
 Binder, B., et al. 2012, ArXiv e-prints  
 Binder, B., et al. 2011, ApJ, 737, 77  
 Bouchard, A., Prugniel, P., Koleva, M., & Sharina, M. 2010, A&A, 513, A54  
 Bozzo, E., Falanga, M., & Stella, L. 2008, ApJ, 683, 1031  
 Broos, P. S., Townsley, L. K., Feigelson, E. D., Getman, K. V., Bauer, F. E., & Garmire, G. P. 2010, ApJ, 714, 1582  
 Canizares, C. R., Fabbiano, G., & Trinchieri, G. 1987, ApJ, 312, 503  
 Cappelluti, N., et al. 2009, A&A, 497, 635  
 Cash, W. 1979, ApJ, 228, 939  
 Dalcanton, J. J., et al. 2009, ApJS, 183, 67  
 del Río, M. S., Brinks, E., & Cepa, J. 2004, AJ, 128, 89  
 Eracleous, M., Shields, J. C., Chartas, G., & Moran, E. C. 2002, ApJ, 565, 108  
 Eracleous, M., Sipior, M. S., & Sigurdsson, S. 2006, in IAU Symposium, Vol. 230, Populations of High Energy Sources in Galaxies, ed. E. J. A. Meurs & G. Fabbiano, 417  
 Evans, I. N., et al. 2010, ApJS, 189, 37  
 Fabbiano, G. 2006, ARA&A, 44, 323  
 Fragos, T., et al. 2008, ApJ, 683, 346  
 Freeman, P. E., Kashyap, V., Rosner, R., & Lamb, D. Q. 2002, ApJS, 138, 185  
 Gehrels, N. 1986, ApJ, 303, 336  
 Georgakakis, A., Nandra, K., Laird, E. S., Aird, J., & Trichas, M. 2008, MNRAS, 388, 1205  
 Gilfanov, M. 2004, MNRAS, 349, 146  
 Grimm, H.-J., Gilfanov, M., & Sunyaev, R. 2002, A&A, 391, 923  
 Grimm, H.-J., Gilfanov, M., & Sunyaev, R. 2003, MNRAS, 339, 793  
 Høg, E., et al. 2000, A&A, 355, L27  
 Humphrey, P. J., Liu, W., & Buote, D. A. 2009, ApJ, 693, 822  
 Kalberla, P. M. W., Burton, W. B., Hartmann, D., Arnal, E. M., Bajaja, E., Morras, R., & Pöppel, W. G. L. 2005, A&A, 440, 775  
 Kilgard, R. E., Kaaret, P., Krauss, M. I., Prestwich, A. H., Raley, M. T., & Zezas, A. 2002, ApJ, 573, 138  
 Kim, D.-W., & Fabbiano, G. 2004, ApJ, 611, 846

TABLE 13  
X-RAY SOURCE PROPERTIES AND CLASSIFICATION

No.	Class from HRs	Spectral Fit	Variability	$d$ (kpc)	Counterparts?	Classification
(1)	(2)	(3)	(4)	(5)	(6)	(7)
1	XRB	pow, $\Gamma = 1.65$	rapid	4.8	UV, optical	AGN
2	XRB	pow, $\Gamma = 0.6$		4.5	none	AGN
3	XRB	pow, $\Gamma = 1.5$		4.3	UV	AGN
4	XRB			4.1	optical, IR	AGN
5	SOFT			3.8	optical	FS
6	XRB			3.8	none	AGN
7	XRB	pow, $\Gamma = 1.8$		4.1	UV, optical	AGN
8	XRB			4.1	radio	AGN
9	XRB			3.3	none	AGN
10	ABS			3.1	none	AGN
11	ABS	pow, $\Gamma = 0.8$		3.5	none	AGN
12	ABS			2.7	none	AGN
13	XRB	pow, $\Gamma = 1.2$		3.4	none	AGN
14	XRB			2.6	none	AGN
15	HARD			3.3	UV	AGN
16	ABS		long	2.4	none	XRB
17	XRB	pow, $\Gamma = 1.9$		2.0	UV, optical	AGN
18	XRB		long	2.0	none	AGN
19	XRB			2.7	UV	AGN
20	XRB	pow, $\Gamma = 1.5$		1.7	UV	AGN?
21	XRB			1.7	UV	AGN?
22	SOFT			2.4	none	XRB
23	ABS			1.6	none	AGN
24	ABS			2.0	none	AGN
25	ABS			1.5	none	AGN
26	XRB			1.4	none	XRB
27	ABS		long?	1.7	UV, <i>HST</i> , optical	AGN?
28	XRB			1.9	UV	AGN?
29	SNR			1.2	UV, <i>HST</i>	SSS?
30	XRB			1.2	none	AGN
31	SOFT			1.3	none	AGN
32	XRB	apec, $kT=0.8$		1.7	UV	SSS?
33	XRB			1.9	none	AGN
34	HARD			0.6	none	XRB
35	ABS	abs. apec, $kT=2.8$		1.6	none	SSS?
36	HARD			0.6	none	AGN
37	HARD		long	0.4	none	XRB
38	XRB			0.3	none	XRB
39	SOFT	pow, $\Gamma = 1.4$		1.4	UV	AGN?
40	ABS		long	1.1	none	XRB
41	XRB	pow, $\Gamma = 2.1$		0.0	UV, IR, radio	NUCLEUS
42	XRB			1.5	none	XRB
43	SNR			0.1	none	SSS?
44	ABS			1.1	UV	AGN
45	SOFT	pow, $\Gamma = 1.6$		1.3	none	AGN
46	XRB	pow, $\Gamma = 1.4$		1.7	none	AGN
47	XRB			0.6	none	XRB
48	XRB			0.6	none	XRB
49	XRB		long?	0.5	none	XRB
50	ABS			1.2	UV	AGN?
51	XRB			1.6	UV, optical, IR	XRB
52	XRB			1.9	UV, optical	XRB
53	SOFT		long	0.9	UV	XRB?
54	XRB		long	1.0	none	AGN
55	XRB	pow, $\Gamma = 0.9$	long	1.7	none	XRB?
56	XRB			1.5	none	XRB
57	XRB		long?	1.7	none	XRB
58	SOFT	pow, $\Gamma = 1.5$		2.1	none	XRB
59	XRB		long	1.9	UV	XRB
60	ABS			2.5	none	XRB



TABLE 13  
X-RAY SOURCE PROPERTIES AND CLASSIFICATION (*continued*)

No.	Class from HRs	Spectral Fit	Variability	$d$ (kpc)	Counterparts?	Classification
(1)	(2)	(3)	(4)	(5)	(6)	(7)
61	XRb		long	2.5	none	XRb
62	ABS			2.6	none	AGN
63	XRb			3.1	none	AGN
64	XRb	pow, $\Gamma = 1.8$	long	3.2	none	AGN
65	SNR	apec, $kT=0.6$		3.1	UV, optical, IR	FS
66	XRb			3.8	UV	AGN
67	XRb	pow, $\Gamma = 1.2$		4.2	UV, optical	AGN
68	XRb	pow, $\Gamma = 1.2$		4.6	optical	AGN
69	SOFT			3.9	IR	AGN
70	XRb	pow, $\Gamma = 1.8$		4.0	UV	AGN
71	XRb		long	4.8	none	AGN
72	XRb	pow, $\Gamma = 1.7$		4.8	UV	AGN
73	ABS	pow, $\Gamma = 1.1$	rapid	4.9	none	AGN
74	XRb			6.3	UV	AGN

- Kim, D.-W., et al. 2009, ApJ, 703, 829  
Kong, A. K. H., & Di Stefano, R. 2003, ApJ, 590, L13  
Kong, A. K. H., Garcia, M. R., Primini, F. A., Murray, S. S., Di Stefano, R., & McClintock, J. E. 2002, ApJ, 577, 738  
Luo, B., et al. 2008, ApJS, 179, 19  
Maíz-Apellániz, J., Cieza, L., & MacKenty, J. W. 2002, AJ, 123, 1307  
Maoz, D., Koratkar, A., Shields, J. C., Ho, L. C., Filippenko, A. V., & Sternberg, A. 1998, AJ, 116, 55  
Maoz, D., Nagar, N. M., Falcke, H., & Wilson, A. S. 2005, ApJ, 625, 699  
Michielsen, D., et al. 2008, MNRAS, 385, 1374  
Nandra, K., et al. 2005, MNRAS, 356, 568  
Napolitano, N. R., et al. 2011, MNRAS, 411, 2035  
O'Sullivan, E., Forbes, D. A., & Ponman, T. J. 2001, MNRAS, 328, 461  
Paczynski, B., & Sienkiewicz, R. 1981, ApJ, 248, L27  
Park, T., Kashyap, V. L., Siemiginowska, A., van Dyk, D. A., Zezas, A., Heinke, C., & Wargelin, B. J. 2006, ApJ, 652, 610  
Paul, B., & Naik, S. 2011, Bulletin of the Astronomical Society of India, 39, 429  
Plucinsky, P. P., et al. 2008, ApJS, 174, 366  
Prestwich, A. H., Kilgard, R. E., Primini, F., McDowell, J. C., & Zezas, A. 2009, ApJ, 705, 1632  
Primini, F. A., Forman, W., & Jones, C. 1993, ApJ, 410, 615  
Revnivtsev, M., Postnov, K., Kuranov, A., & Ritter, H. 2011, A&A, 526, A94  
Ritter, H. 1999, MNRAS, 309, 360  
Seth, A. C., et al. 2010, ApJ, 714, 713  
Shtykovskiy, P. E., & Gilfanov, M. R. 2007, Astronomy Letters, 33, 437  
Skrutskie, M. F., et al. 2006, AJ, 131, 1163  
Smith, R. K., Brickhouse, N. S., Liedahl, D. A., & Raymond, J. C. 2001, ApJ, 556, L91  
Soria, R., & Kong, A. K. H. 2002, ApJ, 572, L33  
Taam, R. E. 1983, ApJ, 270, 694  
Thilker, D. A., et al. 2010, ApJ, 714, L171  
Tikhonov, N. A., Galazutdinova, O. A., & Aparicio, A. 2003, A&A, 401, 863  
Trentham, N., Tully, R. B., & Mahdavi, A. 2006, MNRAS, 369, 1375  
Trudolyubov, S. P., Borozdin, K. N., Priedhorsky, W. C., Mason, K. O., & Cordova, F. A. 2002, ApJ, 571, L17  
Tüllmann, R., et al. 2011, ApJS, 193, 31  
Vaughan, S., Edelson, R., Warwick, R. S., & Uttley, P. 2003, MNRAS, 345, 1271  
Verbunt, F., & Zwaan, C. 1981, A&A, 100, L7  
Voss, R., & Gilfanov, M. 2006, A&A, 447, 71  
Voss, R., & Gilfanov, M. 2007, A&A, 468, 49  
Voss, R., et al. 2009, ApJ, 701, 471  
Wernli, F., Emsellem, E., & Copin, Y. 2002, A&A, 396, 73  
Williams, B. F., Dalcanton, J. J., Gilbert, K. M., Stilp, A., Dolphin, A., Seth, A. C., Weisz, D., & Skillman, E. 2010, ApJ, 716, 71  
Williams, B. F., et al. 2008, ApJ, 680, 1120  
Wilms, J., Allen, A., & McCray, R. 2000, ApJ, 542, 914